

ALMA MATER STUDIORUM · UNIVERSITÀ DI BOLOGNA

---

SCUOLA DI SCIENZE

Corso di Laurea Magistrale in Fisica del Sistema Terra

**Wavelet analysis of downslope flows  
in Materhorn 2012 experiment**

**Relatore:**

**Prof.ssa Silvana Di Sabatino**

**Correlatori:**

**Dr. Laura Sandra Leo**

**Dr. Temistocle Grenga**

**Presentata da:**

**Marco Possega**

**Sessione II**

**Anno Accademico 2018/2019**

# Abstract

In the last years, increasing attention has been devoted to the study of *complex terrain* flows, with the specific goal in achieving a better understanding of air circulation which usually develops over mountainous regions. Progress in this field of research is fundamental for improvements of numerical weather prediction models for irregular topography areas, which are commonplace in human settlements across the world.

Mountainous regions are often characterized by the *diurnal mountain wind system*, a thermally driven circulation involving winds following the shape of the underlying surface, such as, for example, downslope flows which originate during nighttime and travel down the mountain slopes.

Nocturnal downslope flows are investigated in this work, using a subset of experimental data collected at Granite Mountain, in Utah, during MATERHORN campaign. The dataset consists of data measured by sonic anemometers as well as slow sensors mounted up to seven levels on 4 towers deployed along a main lower slope ( $\alpha \approx 2 - 3^\circ$ ) of Granite Mountain.

The study is performed through the Wavelet Transform method, a mathematical tool which improves the classical Fourier Transform, as it provides the location in time and/or space in addition to frequencies of physical phenomena.

The final purpose of the present thesis is to evaluate the ability of Wavelet Analysis of detecting relevant flow features in the flow dynamics and to characterize their behavior.

Wavelet Transform resulted to be an appropriate method to perform this type of study. In particular, it was proved capable of detecting transitions between flow regimes, as well as the presence of flow oscillations at different frequencies. Moreover, it has been efficient in highlighting specific events such as collisions between wind fronts and abrupt variations in measured signals.

# Sommario

Negli ultimi anni, una considerevole attenzione è stata rivolta allo studio dei flussi di vento su terreno complesso, con un interesse particolare nella ricerca di una migliore comprensione delle circolazione tipica delle regioni montuose. I progressi in questo ambito sono fondamentali per il miglioramento dei modelli numerici di previsione del tempo in zone con topografia irregolare, le quali includono una buona parte degli insediamenti urbani.

Le regioni montuose sono caratterizzate dal *diurnal mountain wind system*, vale a dire una circolazione guidata da gradienti termici che coinvolge venti che si muovono seguendo il profilo della superficie, come ad esempio i flussi downslope che si originano durante la notte e si propagano scendendo lungo i pendii delle montagne. In questo lavoro vengono analizzati i flussi downslope notturni, utilizzando in particolare un subset dei dati sperimentali raccolti nella zona della Granite Mountain, nello Utah, durante la campagna MATERHORN. Il dataset consiste in misure effettuate da anemometri sonici e sensori a bassa frequenza installati su 4 torri posizionate lungo un lato della Granite Mountain caratterizzato da leggera pendenza ( $\alpha \approx 2 - 3^\circ$ ).

Lo studio viene realizzato utilizzando il metodo della Trasformata Wavelet, uno strumento matematico che offre miglioramenti rispetto alla classica Trasformata di Fourier, in quanto fornisce la localizzazione temporale e/o spaziale di un segnale fisico in aggiunta alle frequenze.

L'obiettivo finale della tesi è valutare le capacità dell'Analisi Wavelet sia nel rilevare caratteristiche d'interesse nella dinamica dei flussi downslope sia nel descrivere il loro comportamento.

La Trasformata Wavelet è risultata essere uno strumento appropriato nell'eseguire questo tipo di studio. In particolare, ha dimostrato un'elevata abilità nell'individuare periodi di transizione tra diversi regimi del flusso e nel catturare la presenza di oscillazioni a differenti frequenze. Inoltre, si è dimostrato un metodo efficiente nel determinare eventi specifici come collisioni tra diversi fronti di vento e variazioni repentine nei valori dei segnali misurati.

*A Lello  
e Graziella*

# Contents

<b>1</b>	<b>Introduction</b>	<b>5</b>
1.1	Diurnal mountain wind systems . . . . .	6
<b>2</b>	<b>Physics of slope flows</b>	<b>9</b>
2.1	Reynolds-averaged Navier-Stokes equations . . . . .	9
2.2	The role of energy budget and turbulence in slope flows . . . . .	11
2.3	Upslope flows . . . . .	12
2.4	Downslope flows . . . . .	13
<b>3</b>	<b>Methodology: the wavelet transform</b>	<b>18</b>
3.1	Introduction to wavelets . . . . .	18
3.2	Continuous wavelet transform . . . . .	20
3.3	Discrete wavelet transform . . . . .	26
3.4	Some wavelet families . . . . .	28
3.5	Wavelet analysis of complex terrain flows . . . . .	35
<b>4</b>	<b>The experimental setup</b>	<b>37</b>
4.1	The MATERHORN campaign . . . . .	37
4.2	MATERHORN-X, September - October 2012 . . . . .	38
4.3	Data Pre-processing . . . . .	40
4.3.1	Despiking . . . . .	40
4.3.2	Wind data rotation . . . . .	41
<b>5</b>	<b>Data analysis and results</b>	<b>46</b>
5.1	Selection of wavelet family . . . . .	46
5.2	Selection of days and time intervals . . . . .	49
5.3	28 September . . . . .	52
5.3.1	Evening transition . . . . .	53
5.3.2	Downslope regime . . . . .	57
5.3.3	Collision region . . . . .	65
5.4	30 September . . . . .	70
<b>6</b>	<b>Conclusion</b>	<b>74</b>

# Chapter 1

## Introduction

Wavelet transforms (WT) are mathematical techniques which allow to analyze a data signal in time and frequency domains simultaneously. The method was introduced at the beginning of the 1980s [15] as an alternative to the traditional Fourier Transform and represents a powerful tool for the analysis of non-stationary, noisy, intermittent, transient signals. Since its first appearance, WT have found application in many areas of science and engineering [22] and have been used for a wide variety of problems, from heart monitoring [40] to seismic signal denoising [39], from video image compression [32] to the analysis of financial indexes [20], and so on.

In 1992, Farge [15] discussed the use of WT in fluid dynamics, especially in relation to the detection of coherent structures in turbulent flows. Following its first appearance, WT rapidly found application in several geophysics topics, e.g. atmospheric cold fronts [21], dispersion of ocean waves [35], tropical convection [58], wave growth and breaking [33] and El Niño-Southern Oscillation variance on interdecadal time-scales [55].

More recently, WT have been explored by the atmospheric boundary layer research community to study nocturnal boundary flows in complex terrain (e.g. [43], [44], [53] and [54]), which is the topic of this thesis.

Complex terrain is a broad term typically used for sloping terrain (hills, mountains) and irregular topography. More in general, it refers to any type of heterogeneous land surface.

As reported in [49], nearly 70% of the Earth's land surface is characterized by complex terrain. Furthermore, a majority of the world's urban settlements as well as wind farms are placed in mountainous regions, which is why modeling of atmospheric flow over complex terrain is receiving increased attention.

Current modeling limitations are essentially related to the fact that flow and turbulence characteristics over mountainous terrain deviate substantially from the classical boundary layer theory, which relies on (and is strictly limited to) the assumption of flat and homogeneous terrain ([30], [23], [52]). As such, complex terrain boundary layer flows represent an active field of research, and its progress in knowledge has the potential to greatly improve many applications of numerical weather prediction (NWP), including air quality modeling, emergency response, dispersion modeling, and wind energy forecasting in mountainous areas ([4], [61], [11]).

The present thesis focuses on a specific category of complex terrain flows, name-

ly downslope flows. The goal is assessing the ability of WT in capturing their characteristics and evolution using field observations collected during the Mountain Terrain Atmospheric Modeling and Observations (MATERHORN) campaign at Granite Mountain, Utah [16]. The present thesis is divided in 5 chapters:

- 1) In the remaining part of Chapter 1, a brief overview of complex terrain circulation is provided;
- 2) Chapter 2 provides a theoretical and phenomenological discussion on the typical slope flow circulation, with a focus on downslope flows, which supplies the necessary background for the present work;
- 3) Chapter 3 introduces the theory of wavelet and its mathematical formalism. It provides an overview of wavelet transform in its two possible variants, i.e. continuous WT (CWT) and discrete WT (DWT), with some examples regarding a few wavelet families. The chapter concludes with a summary on the scientific literature dealing with the application of wavelet analysis to complex terrain flows;
- 4) Chapter 4 provides an overview the MATERHORN campaign, followed by a description of the experimental apparatus and specific dataset exploited for this work;
- 5) Chapter 5 deals with the specific analysis carried out in the present thesis and discuss the main outcomes of it;
- 6) Finally, Chapter 6 summarizes the entire work, recapping the results obtained and providing suggestions for future studies.

## 1.1 Diurnal mountain wind systems

Air circulation over mountainous landscapes is mainly governed by two mechanisms, as mentioned in [59]. The first one is driven by the synoptic forcing produced by large-scale pressure gradients, while the second consists of the thermal circulation associated with the diurnal cycle of heating and cooling of the lower atmospheric layers. This latter mechanism principally drives the *diurnal mountain wind system*, i.e. the thermally driven circulation forming over lands with relevant orographic features under fair weather conditions, when skies are clear and winds aloft are weak. Depending on the topography spatial dimensions (e.g. small hills vs large mountain massifs) and other parameters, diurnal mountain wind systems may develop at different spatial and temporal scales, and have different characteristics in terms of flow speed, depth, duration and onset times. However, all of them share the property of twice a day wind direction reversal.

Diurnal mountain winds are driven by horizontal temperature differences, and their evolution is strictly dependent on the thermal structure of the atmospheric boundary layer within the valley, which is characterized by a diurnal cycle of buildup and breakdown of a temperature inversion. These temperature gradient leads to a pressure gradient which produces wind flows from high to low pressure regions.

Such circulations are then closed by return or compensatory flows.

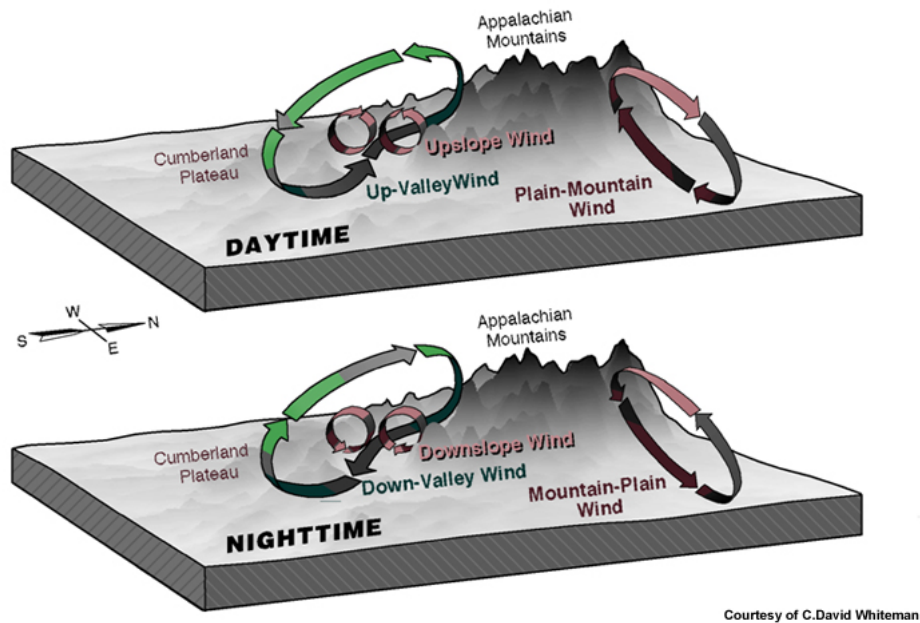


Fig. 1.1: Representation of a typical Diurnal wind system circulation. [59]

Figure 1.1, taken from [59], shows a typical circulation established over a mountainous area. In particular, all the characteristic flows are depicted: *upslope* or *anabatic* wind, *up-valley* wind and *plain-to-mountain* wind developing during daytime, whilst *downslope* or *katabatic* wind, *down-valley* wind and *mountain-to-plain* wind forming during nighttime in the opposite direction. *Slope* flows are buoyancy circulations following the inclination of the underlying slope and are caused by differences in temperature between air heated during daytime or cooled during nighttime over the mountain slopes and air at the same altitude over the valley center. *Valley* flows are closed circulations along the valley axis connected with the horizontal pressure gradients between air columns with different temperature structures over a valley and the adjacent plain. *Mountain-to-plain* and *plain-to-mountain* winds are produced by the daily heating and cooling contrast between the atmospheric layers over the external slopes of a mountain massif and the free atmosphere over the surrounding plain.

The behavior of these complex terrain circulations has captured the interest of many researchers during last two decades, and several improvements have been achieved in this field. Knowledge about mountainous wind systems is widely described in [7], where state-of-the-art theoretical models, parametrizations and observations are reported. However, progress in research and knowledge of complex terrain flows is limited by the fact that these flows are rarely observed in nature in their pure form, whereas their characteristics are site-dependent. Since almost infinitely possible terrain configurations exist, results from experiments and numerical simulations are strictly valid only for the single specific case analyzed and therefore difficult to generalize beyond the case. Nevertheless, scientific community progress derives from

studies relative to situations with similar ground conditions and/or terrain configurations, from which general information for what concerns the fundamental physical mechanisms are deduced.

# Chapter 2

## Physics of slope flows

The definition *slope flow* usually refer to winds blowing along a slope of a hill or a mountain. Upslope or *anabatic* wind generally flows during daytime when the surface receives solar radiation. The air layers near the ground become warmer than the environment air at the same elevation, then this temperature difference produces density difference which results in buoyancy forces making the air ascend the slope. Conversely, downslope or *katabatic* wind develops when nocturnal boundary layer gets cooler due to heat loss and flows down the slope. As mentioned before, these temperature deficits are connected with density gradients which drive the flows, with the maximum effect near the surface where radiative processes are more powerful. Although the buoyancy force strongly acts in the proximity of the surface, the opposite contribution of the surface friction decelerates the wind speed, which reaches zero at the ground. The combination of these two factors produces a typical low level jet profile (so called "nose") in both downslope and upslope wind regimes whose velocity maximum, with value in the range between 1 and 5 m/s, is located above the surface (at typical height ranging from 1 to 15 m for downslope flows and from 10 to 50 m above the surface for upslope flows).

### 2.1 Reynolds-averaged Navier-Stokes equations

Dynamics of slope flows is described by Navier-Stokes (N-S) equations. In order to take into account the turbulent nature of these flows, usually Reynolds decomposition of instantaneous quantities appearing in N-S equations is employed. Reynolds decomposition involves the separation of a flow instantaneous variable into the mean component and the fluctuating component, namely

$$u(\mathbf{x}, t) = U(\mathbf{x}) + u'(\mathbf{x}, t), \quad (2.1)$$

where  $\mathbf{x} = (x, y, z)$  is the position vector and time-averaged  $U$  is

$$U(\mathbf{x}) = \frac{1}{\Delta t} \int_t^{t+\Delta t} u(\mathbf{x}, t) dt. \quad (2.2)$$

Starting from N-S equations, exploiting the aforementioned mathematical tool and time-averaging the resulting equation, a set of Reynolds-averaged Navier-Stokes

(RANS) equations is obtained. This set of simplified equations is usually adopted to provide a general comprehension of physics of slope flows.

Following [62], define a cartesian coordinate system as in Fig. 2.1, where angle  $\alpha$  is the inclination of the slope,  $s$  is downslope direction and  $n$  is orthogonal to the slope and increasing upward.

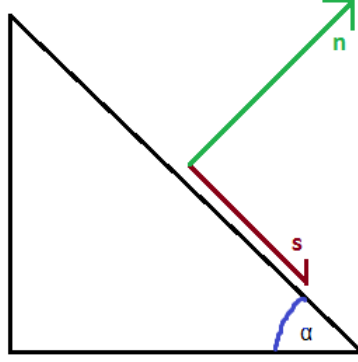


Fig. 2.1: Downslope reference system.

The potential temperature, i.e. the temperature which an air parcel would reach if adiabatically brought to a standard reference pressure (generally 1 atm), can be written in this reference system as

$$\theta = \theta_0 + \gamma z + \delta(s, n, t), \quad (2.3)$$

where  $\theta_0$  is the value of  $\theta$  at the ground without heat sources,  $\gamma$  is the potential temperature lapse rate,  $z = n \cos \alpha - s \sin \alpha$  and  $\delta$  represents the perturbation near the slope. Designating with  $u$  and  $w$  the  $s$ -component and the  $n$ -component respectively, the mean along-slope equation of motion for a 2-dimensional and cross-slope invariant flow is

$$\frac{\partial U}{\partial t} + U \frac{\partial U}{\partial s} + W \frac{\partial U}{\partial n} = -\frac{1}{\rho_0} \frac{\partial(p - p_a)}{\partial s} - g \frac{\delta}{\theta_0} \sin \alpha - \frac{\overline{\partial u' w'}}{\partial n}, \quad (2.4)$$

while the mean slope-perpendicular equation of motion is

$$\frac{\partial W}{\partial t} + U \frac{\partial W}{\partial s} + W \frac{\partial W}{\partial n} = -\frac{1}{\rho_0} \frac{\partial(p - p_a)}{\partial n} + g \frac{\delta}{\theta_0} \cos \alpha, \quad (2.5)$$

where  $\rho_0$  is reference density independent of surface cooling mechanism,  $p_a$  is the ambient pressure retrieved from the hydrostatic equation,  $u'$  and  $w'$  are the fluctuations of velocity components. Often right-hand side of Eq 2.5 is considered negligible assuming zero slope-perpendicular accelerations, which result in quasi-hydrostatic balance. Using the Boussinesq approximation the continuity equation is

$$\frac{\partial U}{\partial s} + \frac{\partial W}{\partial n} = 0, \quad (2.6)$$

which implies a balance between divergences of the two component of the flow. The thermodynamic energy equation can be written as

$$\frac{\partial \theta}{\partial t} + U \frac{\partial \theta}{\partial s} + W \frac{\partial \theta}{\partial n} = -\frac{1}{\rho_0 c_p} \frac{\partial R}{\partial n} - \frac{\overline{\partial \theta' w'}}{\partial n}, \quad (2.7)$$

where  $c_p$  is the specific heat of air keeping pressure fixed and  $R$  represents the upward radiative flux. The first term on right-hand side of Eq. 2.7 connects radiative heat source with temperature variation, while the second term on right-hand side is due to RANS approximation and relates temperature and  $w$  fluctuations. These factors produce the temperature gradient over the slope that generates the buoyancy force capable of driving the entire flow.

A solution to the set of RANS equations can be found numerically, but it is common to simplify those equations retaining only the essential terms, in order to obtain a set which is possible to solve analytically. One example of this simplified model will be presented later.

## 2.2 The role of energy budget and turbulence in slope flows

As anticipated at the beginning of this section, the main force driving slope winds is the generation of temperature gradients along the terrain, which are linked to the heat fluxes at that locations in agreement with energy conservation. The potential temperature tendency equation [62] is

$$\frac{\partial}{\partial t}(\rho c_p \theta) = -\nabla \cdot \mathbf{S} - \nabla \cdot \mathbf{F} - \frac{\theta}{T} \nabla \cdot \mathbf{R}. \quad (2.8)$$

It is possible to notice that potential temperature variations depend on sensible heat flux  $S = \rho c_p \mathbf{u} \theta$  related to local advection of air, on turbulent sensible heat flux  $F = \rho c_p \overline{\mathbf{u}' \theta'}$  associated with wind velocity and potential temperature covariance and on the radiative heat flux  $R$ . Even though  $S$  is not negligible, the predominant inputs are provided by the other two factors, in particular by their divergences which cool or heat the layer over a slope and produce a buoyancy force capable of moving downslope or upslope flows.

Sensible heat fluxes are substantially influenced by the effect of turbulence. The coupling activity of the vertical wind shear and the momentum flux constantly produces last terms in Eq. 2.4 and 2.7 in slope flows. Following the coordinate system described in Fig. 2.4, the TKE equation [24] can be written as

$$\frac{\partial \bar{e}}{\partial t} = -\overline{u'w'} \left( \frac{\partial U}{\partial n} \right) + \frac{g}{\theta} (\overline{w'\theta'_v} \cos \alpha - \overline{u'\theta'_v} \sin \alpha) - T - \epsilon, \quad (2.9)$$

where  $e = (u'^2 + v'^2 + w'^2)/2$  is the TKE,  $\epsilon$  is the dissipation rate of the TKE,  $\theta_v$  is the virtual potential temperature (the theoretical potential temperature of dry air

which would have the same density as moist air) and  $T$  contains the transport and pressure work terms. Second term on right-hand side represents the sum of vertical components of the slope-normal and along-slope density fluxes, with the  $\overline{u'\theta'_v} \sin \alpha$  factor which increases or reduces turbulence amount depending on its position along the "nose" shape of the velocity vertical profile. In detail, in the layer below the wind maximum an upward moving air parcel turns out to be slower ( $u < 0$ ) and cooler ( $\theta < 0$ ) than its surroundings, while a downward moving air parcel is faster ( $u > 0$ ) and warmer ( $\theta > 0$ ). Thus, in this layer, contribution to the along-slope heat flux is positive ( $\overline{u'\theta'} > 0$ ). Following the same reasoning, it is simple to demonstrate that this contribution is instead negative ( $\overline{u'\theta'} < 0$ ) in the region above the flow wind maximum.

### 2.3 Upslope flows

The following figure taken from [62] shows the classic shape of wind and temperature profile for upslope flows.

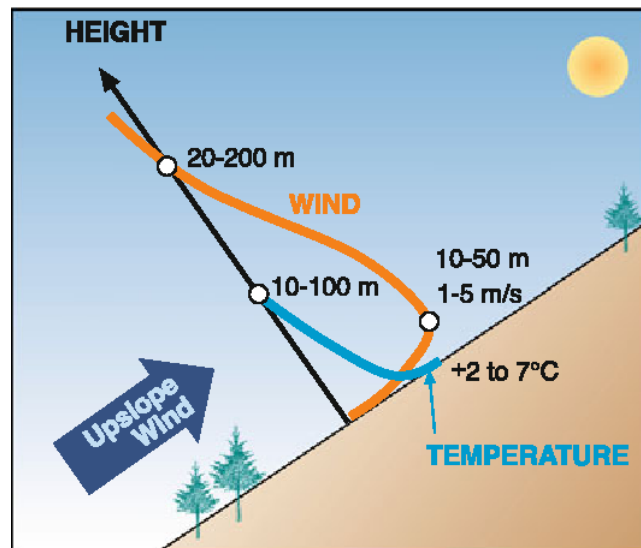


Fig. 2.2: Conventional wind and temperature profiles for upslope flows. Characteristic features of the temperature excess layer, the wind speed and its peak's elevation and the depth of the upslope flow layer are reported.[62]

Upslope flows generally form after sunrise, when surface is heated by radiative sources and the induced upward sensible heat fluxes grow. Since the heat flux constantly enhances during daytime, it is impossible for an upslope flow to reach a steady state. In the morning a thermally stable air layer developed during night lies above the upslope flow, and when the slope starts to get warmed a convective boundary layer arises. Due to the slanted surface, also advection is important, so convective air parcels move following the slope. Depth and intensity of the upslope flow rapidly increases after sunrise, whereas air enters from the top of the flow while it advances producing an increment of the volume flow until convective air makes an intrusion in the stable layer. After breaking the stable air boundary, the convective-advective air begins to rise upwards and following the slope.

Some interesting features of upslope flows derive from Schumannndlr simulations realized for ideal slopes [46], [62] and can be summarized as:

- The stationary state requires balance between surface friction and buoyancy forces in along-slope momentum equation (Eq. 2.4), while in thermodynamic equation (Eq. 2.7) is necessary to equate the surface heating and the upslope heat advection against the mean temperature gradient;
- Temperature diminishes with height quasi-adiabatically, such as temperature excess also decreases with altitude;
- Largest depth and volume fluxes are typical over low-angle slopes, the opposite happens for steep slopes;
- Velocity shows maximum value within 50 m from the slope surface;
- Momentum is transported upward and downward in slope-normal direction respectively below and above the jet maximum due to the velocity shear values.

## 2.4 Downslope flows

After sunset, usually a transition from upslope to downslope flows occurs. These evening-transition happens with a mechanism which is not completely understood, in particular two possible procedures are suggested in [17]. The first one is the *sliding slab*, which is [31] a development of the downslope flow over the whole slope surface, while the second is called *transition front* and hypothesizes the presence of a stagnation front which moves along the slope raising the upslope-flow layer and removing it from the surface.



In Fig. 2.4, directions of  $s$ ,  $n$  and  $z$  coincide with the coordinates of Fig. 2.1, and  $\alpha$  is the inclination angle.  $\theta_{va}$  and  $\theta_{vR}$  are equal to  $\theta$  and  $\theta_0$  of Eq. 2.3, and  $\delta$  is the same quantity.  $H$  is the characteristic thickness of the layer where katabatic flow is driven by buoyancy forces, while  $h$  is the characteristic thickness of the velocity profile depending on turbulence in the layer. It is useful to define with  $\bar{U}$  the layer-averaged velocity

$$\bar{U} = \frac{1}{h} \int_0^H u dn, \quad (2.10)$$

with  $\Delta$  the layer-averaged buoyancy

$$\Delta = \frac{1}{h} \int_0^H g' dn, \quad (2.11)$$

where  $g' = g\delta/\theta_{vR}$  is the reduced gravity, and to choose the parametrization as in [34]

$$(\overline{u'w'})_0 = -C_D \bar{U}^2, \quad (2.12)$$

where parameter  $C_D$  varying for every specific case. Using relations

$$S_1 \Delta h^2 = 2 \int_0^H g' n dn, \quad (2.13)$$

$$S_2 \Delta h = \int_0^H g' dn, \quad (2.14)$$

$$\int_0^H w dn = H w_H - H S_3 w_H, \quad (2.15)$$

Eq. 2.4 becomes

$$\frac{\partial \bar{U} h}{\partial t} + \frac{\partial \bar{U}^2 h}{\partial s} = -\frac{\partial}{\partial s} \left( \frac{1}{2} S_1 \Delta h^2 \cos \alpha \right) + S_2 \Delta h \sin \alpha - C_D \bar{U}^2 - (\overline{u'w'})_H, \quad (2.16)$$

while Eq. 2.7 can be rewritten as

$$\frac{\partial}{\partial t} (S_2 \Delta h) + \bar{U} h N^2 (\sin \alpha - S_3 E \cos \alpha) + \frac{\partial}{\partial s} (\bar{U} \Delta h) = B_0 - (\overline{g'w'})_H, \quad (2.17)$$

where  $N = \sqrt{g\gamma/\theta_{vR}}$  is the buoyancy frequency,  $E = -w_H/\bar{U}$  is the entrainment coefficient and  $B_0 = g[(R_H - R_0) - Q_0]/(\rho c_p \theta_{vR})$ , in which  $(R_H - R_0)$  is the radiation flux divergence over height  $H$  and  $Q_0 = \rho c_p (\overline{\theta'w'})_0$  is the ground heat flux.

Naming  $L_H$  the length along the slope of the flow and  $\tau = \sqrt{L_H/\Delta \sin \alpha}$  its time scale, observing the left-hand side of 2.16 it is reasonable to consider negligible the unsteady term for processes with time scales for which the inequality  $L_H/\bar{U}\tau \ll 1$  holds. Consequently it is valid to assume the principal inertia-buoyancy balance of forces suggested in [10], i.e.

$$\frac{\bar{U}^2 h}{L_H} \sim \Delta h \sin \alpha, \quad (2.18)$$

which allows to write a velocity scale for katabatic winds as

$$\bar{U} = \lambda_u (\Delta L_H \sin \alpha)^{1/2}, \quad (2.19)$$

being  $\lambda_u$  an empirical constant.

Another important feature appears for time scales shorter than  $\tau$ . In these case the unsteady term is prevailing in Eq. 2.16 and at night the entrainment contribution becomes insignificant, so that Eq. 2.16 and 2.17 can be approximated respectively as

$$\frac{\partial \bar{U}h}{\partial t} \approx \Delta h \sin \alpha \quad (2.20)$$

and

$$\frac{\partial}{\partial t}(\Delta h) + N^2(\bar{U}h) \sin \alpha \approx B_0. \quad (2.21)$$

It is crucial to remark that the solution for the system composed by the two previous equations contains an oscillatory component with a time period equal to

$$T = \frac{2\pi}{N \sin \alpha} \quad (2.22)$$

which characterizes the internal waves arriving perpendicular to the slope.

Moreover, it is possible to define the characteristic scale for the katabatic-layer thickness. Under many assumptions, e.g. high Richardson number, quasi steadiness, relatively small  $N$  and large entrainment coefficient, boundary shallow layer approximation and negligible  $B_0$  compared to  $E$ , the layer thickness at position  $s$  along the slope can be written as

$$h^2(s) = h_0^2 + \frac{3}{2}\lambda_u^2 A s^2 \tan \alpha, \quad (2.23)$$

where  $h_0$  is the thickness at reference location  $s_0$ ,  $\lambda_u$  is a parameter to be determined empirically and  $A \approx 3 \times 10^{-2}$ .

Downslope flow's behavior is influenced by many factors, first of all the slope angle. For this kind of flows, air goes down along the slope only if it is negatively buoyant compared to the environment. However, during the descent air gets warmed following the adiabatic lapse rate (9.8 C°/km) and, since usually there is not a source of cold air which constantly feeds the flow, the downslope motion can continue only thanks to the cooling provided by the downward sensible heat flux to the cold nocturnal surface. If slope angles are low, the distance needed to lose heat through this process is greater than for a steeper slope, and this is why the trajectories on shallow slopes are much longer. Nonetheless, intermediate slope angle are necessary to generate the most intense flows, which are compromises between the magnitude of the gravity vector and the outgoing infrared emission that leads the sensible heat flux.

Also ambient stability affects the flow. If, for example, ambient stability suddenly becomes more intense, in order to maintain its speed the flow has to be cooled faster. Moreover, even inhomogeneities of slope are crucial for downslope flows because they correspond to spatially changes in radiative and turbulent fluxes which reflect on variations in the flows.

Last element influencing this type of flows is the background flow. Since the downslope flow is normally weak, it is often subject to the impact of other flows which can travel in opposite direction or even cross-slope. The most active on downslope flows moving on valley sidewalls are the valley flows. The ordinary jet-like velocity profile characterizes both the vertical and the horizontal cross sections of valley flows, causing horizontal shears varying with height over the slope. Valley winds are mainly oriented along the valley axis, orthogonally to the slope ones, so their effect is to create a directional shear through the slope flow layer, and if they become really powerful they can substantially reshape the downslope flows.

Validity of RANS theoretical models has been tested during several field campaigns, e.g. [60], [5] and [28], finding agreement between predicted behavior and observations. Other methods have been also employed for this kind of study, such as Large Eddy Simulation (LES) [47], [6] or laboratory tank models [45], [48], obtaining remarkable results. Experimental data have been investigated through different techniques, from classical statistical approaches and Fourier analysis to more advanced procedures as multiresolution flux decomposition (MRFD) [29]. The present work is based on the Wavelet Transform method, a relatively recent mathematical tool which has found many applications during the last years and which will be discussed in the next chapter.

# Chapter 3

## Methodology: the wavelet transform

### 3.1 Introduction to wavelets

There are many ways to analyze data trying to extrapolate information about the harmonic components contained in it. The most common is probably the Fourier Transform (FT) or Fast Fourier Transform, which is a computationally effective implemented algorithm of FT. This technique has been widely exploited in many scientific fields due to its simplicity in providing frequency spectral details of any kind of signal. The FT of a function  $f(t)$  can be defined as

$$F_{FT}(\omega) = \int_{-\infty}^{+\infty} f(t)e^{-i\omega t} dt, \quad (3.1)$$

where  $i$  is the imaginary unit and  $\omega$  is the angular frequency. From this definition it is immediately clear that this tool can be ideal if the statistical properties of the signal do not change with time. Indeed, since the basis function, the complex sinusoid  $e^{-i\omega t}$ , exists for  $-\infty < t < +\infty$ , the FT decomposes a time signal into independent harmonic components and, therefore, the function  $F_{FT}(\omega)$  can provide a high resolution identification of frequencies intrinsic to signal without determining their temporal localization. In other words, the FT can correctly detect the frequencies composing the signal, but yields no information about the time location of those features.

The first solution to FT's limitations was suggested by the physicist Dennis Gabor in 1946 [19]. He defined the windowed Fourier Transform or Short-time Fourier Transform (STFT). It consists of multiplying the signal  $f(t)$  with a short (compared to the temporal length of the signal) window function  $g(t - \tau)$ , centered at time  $\tau$ , and calculating the FT of the product  $f(t)g(t - \tau)$ :

$$F_{STFT}(\omega) = \int_{-\infty}^{+\infty} f(t)g(t - \tau)e^{-i\omega t} dt. \quad (3.2)$$

Therefore, the FT of function  $f(t)$  weighted by  $g(t - \tau)$  on time intervals with dimension equal to the compact support of  $w$  is performed. This computation

provides an evaluation of the frequency content of the signal in the neighborhood of  $\tau$ . Thus STFT is the first attempt to obtain a time-frequency analysis of a non-stationary signal. Gabor chose the Gaussian function as the window function,

$$w(t - \tau) = e^{[-(t-\tau)^2]/\sigma^2}, \quad (3.3)$$

which is known as "Gabor Transform".

The STFT does not solve all the problems of a time-dependent frequency behavior of the signal. In particular, the main constraint of this procedure consists in the uniformity of the window for all frequencies. Once the dimension of the window has been chosen, that must be applied to study all the signal, causing many issues in interpreting the analysis. These problems can be understood looking at the Fig. 3.1 and 3.2.

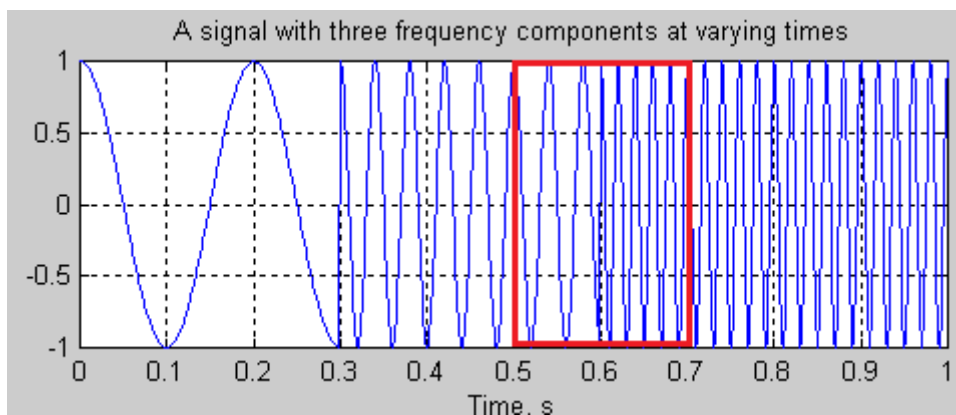


Fig. 3.1: Signal with time-dependent periodicity, the red box is a too large STFT window.

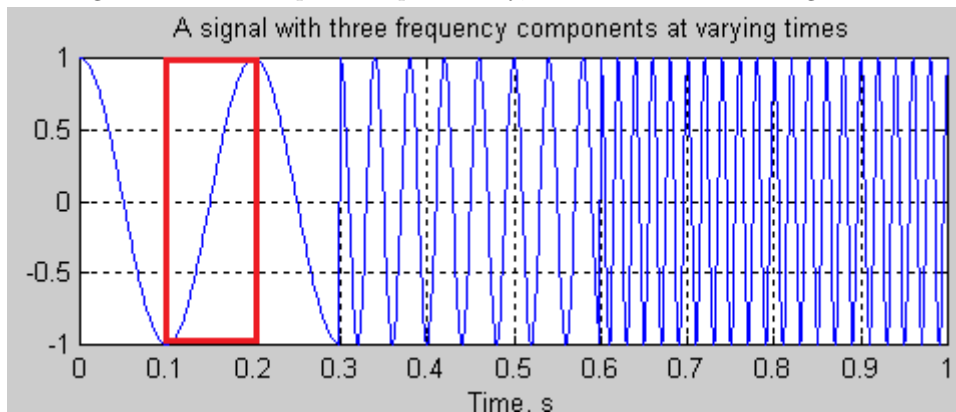


Fig. 3.2: Signal with time-dependent periodicity, the red box is a too short STFT window.

Fig. 3.1 shows the complication for high frequencies due to a large window: the window contains too many different frequencies at different times, a shorter window would be more appropriate. On the other hand, figure 3.2 represents the opposite problem for the low frequencies: the window is too short and cannot detect the periodicity of the signal. What establish the above mentioned constrains for this theory is the uncertainty principle

$$\delta t \delta \omega = 1/2, \quad (3.4)$$

where  $\delta t$  is the transform resolution in time domain and  $\delta\omega$  is the transform resolution in frequency domain. This rule has to be considered for the choice of the window, which must be selected in agreement with the purpose of the analysis. However, since both of these elements remain constant in a STFT analysis, the STFT covers the time-frequency plane with a uniform array of resolution squares, and does not allow an appropriate analysis for a non-stationary signal.

In order to overcome these issues, in the mid-1970s a French geophysicist called Jean Morlet found a solution during his studies in seismology [36]. Following the idea of a time-frequency domain suggested by Gabor, he tried to analyze signal using shortwaves for high frequencies and longwaves for low frequencies. He gave them the name of "wavelets" and defined them starting from a fixed function and manipulating it with dilations. Later, in the 1980s, the theoretical physicist Alex Grossmann [26] discovered the link between Morlet formalism and his own studies regarding coherent states in quantum mechanics. Finally, the joint work of Gabor, Morlet and Grossmann led to the mathematical definition of the Continuous Wavelet Transform (CWT) [25], which will be discussed in the next section.

## 3.2 Continuous wavelet transform

In order to understand the CWT, it is first necessary to give an appropriate definition of *wavelet*. According to [3], "a wavelet is a localized wavelike function used to transform the signal under investigation into another representation which presents the signal information in a more useful form". From a mathematical point of view, a wavelet is a function  $\psi(t)$  with norm equal to 1 satisfying three precise criteria, which are:

- wavelet must have finite energy,

$$E = \int_{-\infty}^{+\infty} |\psi(t)|^2 dt < +\infty, \quad (3.5)$$

where the vertical brackets represent the modulus operator which gives the magnitude of  $\psi(t)$ .

- the Fourier transform of a wavelet  $\psi(t)$ , that is

$$\Psi(f) = \int_{-\infty}^{+\infty} \psi(t)e^{-i2\pi ft} dt, \quad (3.6)$$

must satisfy the *admissibility condition*

$$C = \int_0^{+\infty} \frac{|\Psi(f)|^2}{f} df < +\infty. \quad (3.7)$$

This condition implicitly requires that the wavelet must have a zero mean.

- a Fourier transform of a complex wavelet must be real and vanish for negative frequencies.

A large variety of wavelets exists, of which Fig. 3.3 shows four examples.

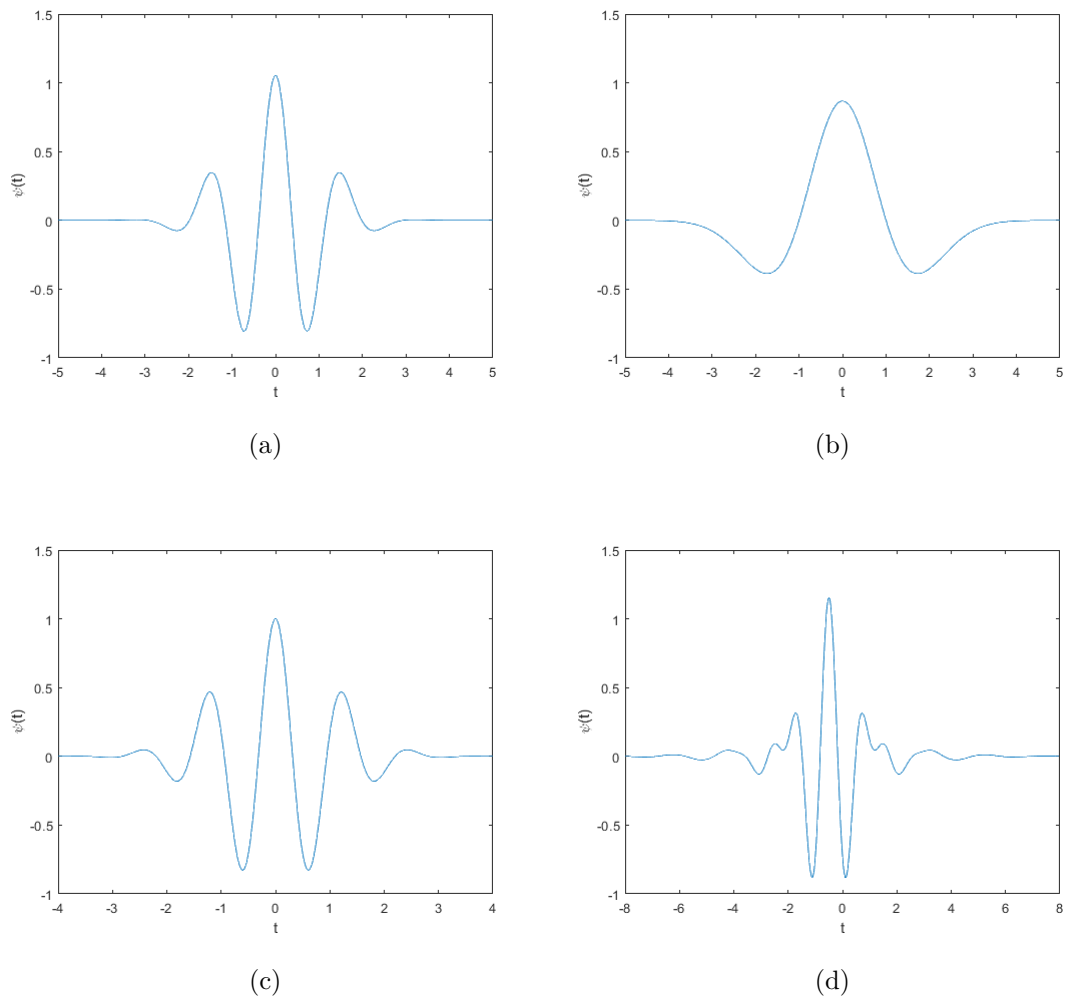


Fig. 3.3: Four wavelets: (a) Gaussian wavelet (first derivative of a Gaussian); (b) Mexican hat (second derivative of a Gaussian); (c) Morlet (real part); (d) Meyer.

Every family of wavelets has features which make it the best one for a particular application, depending on both the characteristics of the signal and what is desirable to retrieve from the analysis, but theoretically all choices are possible. Some wavelet families often employed are described in section 3.4.

The process of wavelet alteration consists of two actions, dilation and translation of a base wavelet function called mother wavelet. The first one literally expands/reduces the domain where the wavelet has non-zero values through the introduction of the *dilation parameter*  $a$  (generally called *scale*), which can be defined in several ways (e.g. for the Mexican hat wavelet is the distance between the center of the wavelet and its crossing of the time axis); while the latter modifies the position of the wavelet along the domain by changing the *location parameter*  $b$ , i.e. the wavelet's center of symmetry. The parameter  $a$  has a dilatation effect when  $a > 1$ , and a contraction effect when  $0 < a < 1$  on the mother wavelet function. It can be modified to analyze the long/short period features of the signal or the low/high frequency aspects of it; while  $b$  determines the position of the wavelet in time domain and thus defines which part of the signal is being analyzed.

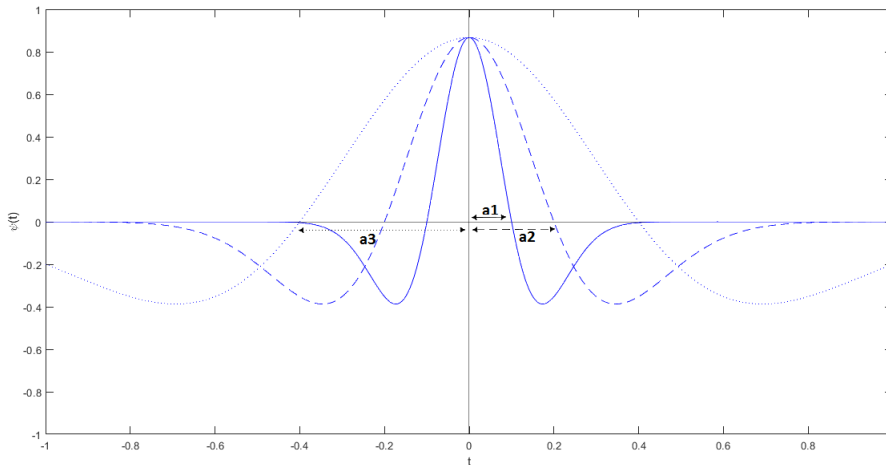


Fig. 3.4: Mexican Hat wavelet: dilation varying  $a$  parameter:  $a_1 = a_2/2$  and  $a_3 = a_2 \times 2$ .

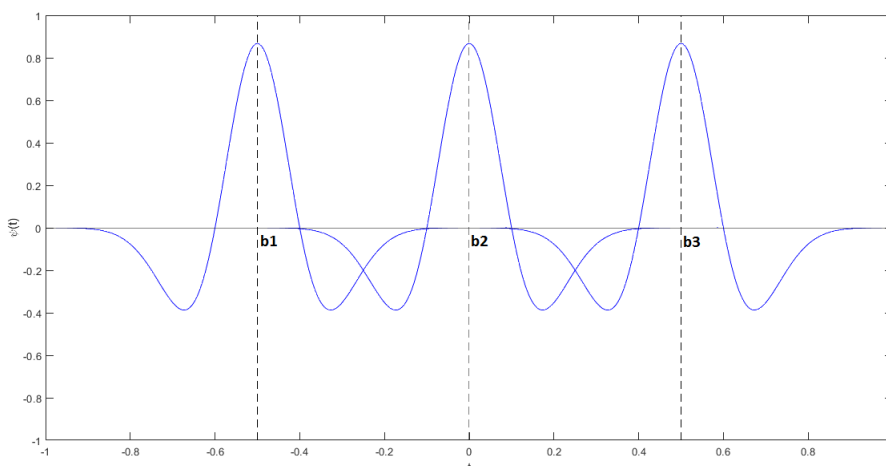


Fig. 3.5: Mexican Hat wavelet: translation varying  $b$  parameter.

Including these two parameters, we can rewrite the *daughter wavelet* as

$$\psi_{a,b}(t) = w(a)\psi\left(\frac{t-b}{a}\right), \quad (3.8)$$

where  $w(a)$  is a weighting function usually set to  $1/\sqrt{a}$  in order to have same energy value at all scales. Note that the mother wavelet is just a daughter wavelet with  $a = 1$  and  $b = 0$ . Adopting the same notation as [3], now it is possible define the *wavelet transform* of a time series  $f(t)$  with respect to the wavelet function as the convolution between  $f$  and the wavelet, namely

$$T(a,b) = \frac{1}{\sqrt{a}} \int_{-\infty}^{+\infty} f(t)\psi^*\left(\frac{t-b}{a}\right)dt, \quad (3.9)$$

where the symbol "\*" stands for the complex conjugate. Thinking that theoretically the dilation and translation parameters may assume continuous values, this is called CWT. Since the basis functions of the CWT are scaled with respect to frequency, wavelets at high frequencies have short domain support, so they present a good time resolution, whereas wavelets at low frequencies exhibit a good frequency resolution in agreement with the uncertainty principle. This varying window structure is an important feature of the CWT, and it is the one which delineates a crucial step forward compared to the STFT. In fact, whilst the ideal partition of the time-frequency plane in the case of STFT is depicted by identical squares, for the CWT it is characterized by rectangles (Fig. 3.6 taken from [51]).

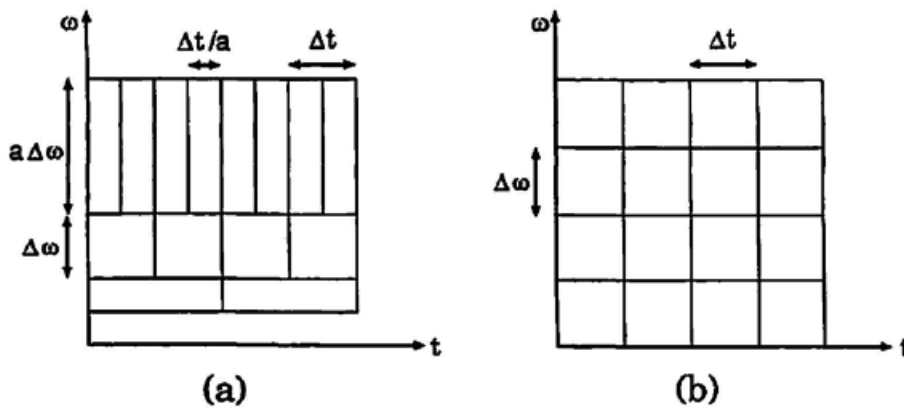


Fig. 3.6: The rectangular resolution of the CWT on the time-frequency plane ( $\omega = 2\pi f$ ), where  $\Delta t$  and  $\Delta\omega$  are respectively the spectral and time width and  $a$  is the scaling parameter. (b) The corresponding square resolution of the STFT.[51]

To easily understand how the CWT works in analyzing a signal, it may be helpful to observe Fig. 3.7 taken from [3], in which a wavelet is superimposed on top of an hypothetical signal.

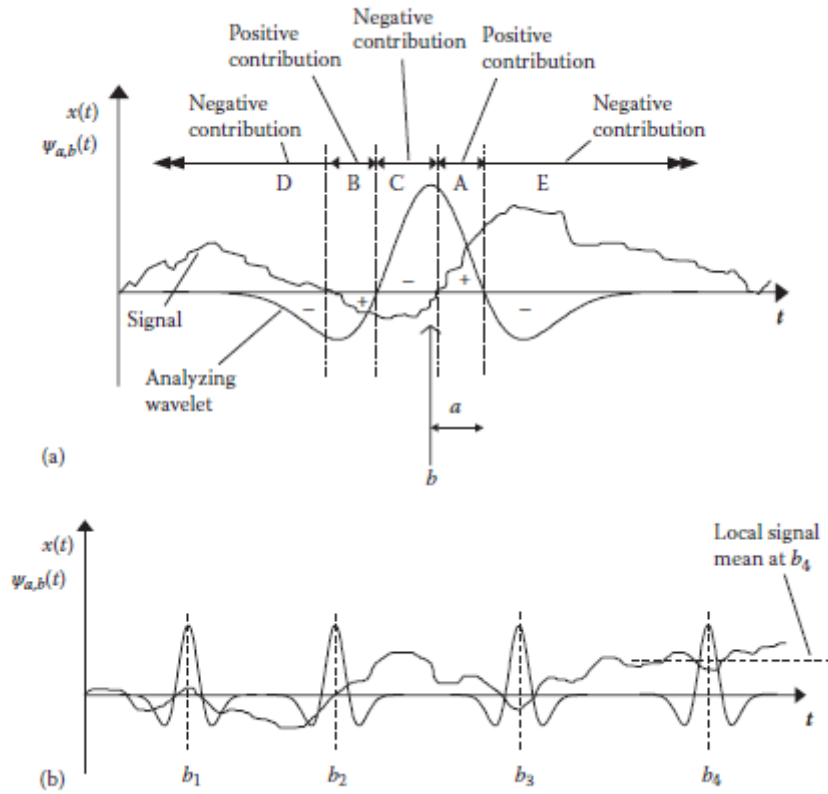


Fig. 3.7: (a) Hypothetical signal with a wavelet superimposed. The symbols + and - represents the zones where the contributions to the integral are respectively positive and negative. (b) A wavelet of fixed  $a$  at four distinct locations on the signal.[3]

Looking at Fig. 3.7(a), it is simple to observe that in regions where the values of the wavelet and the signal are of the same sign the contribution to the integral of Eq 3.9 (region A and B) is positive, while if the signal and wavelet are of opposite sign (regions C, D and E) the contributions to the integral are negative. The effect of varying the location parameter  $b$  is explained graphically in Fig. 3.7(b) for four values of  $b$  ( $b = b_1, b_2, b_3, b_4$ ), while  $a$  is kept constant. Varying  $b$  allows the wavelet to move along the signal. At  $t = b_1$ , the position of the wavelet is such that the positive and negative parts of the signal are more or less coincidental with those of the wavelet, resulting in a large positive value of  $T(a, b)$ . The opposite happens at  $b_3$ : being the signal and the wavelet out of phase, values of  $T(a, b)$  are considerable but negative here.  $T(a, b)$  assumes the lowest at  $b_2$ , because the positive and negative contributions to the integral cancel reciprocally. Case  $b_4$  might be similar to  $b_3$ , but here the signal in the neighborhood of the wavelet reveals a remarkable local mean component which provides to  $T(a, b)$  equally positive and negative contributions. In summary, the mean feature is not emphasized, contrarily to the local component which remains the only one caught by the CWT. Thus shifting the wavelet along the signal is feasible to detect coherent structures relating to a specific a frequency. Repeating this process by varying  $a$  allows to find coherent structures of different frequencies within the signal.

Since performing the CWT of a signal leads to the computation of a wavelet coefficient for every given set of the  $a$  and  $b$  parameters, the results are often represented as a contour plot on an  $a$ - $b$  plane with colors representing the intensities of the transform at each point of such plane. This kind of plot is shown in the following Figures, which represent a simple example of the CWT application to a sinusoidal signal  $f$  of period  $p = 15$  min, namely  $f = \sin(2\pi t/p)$ .

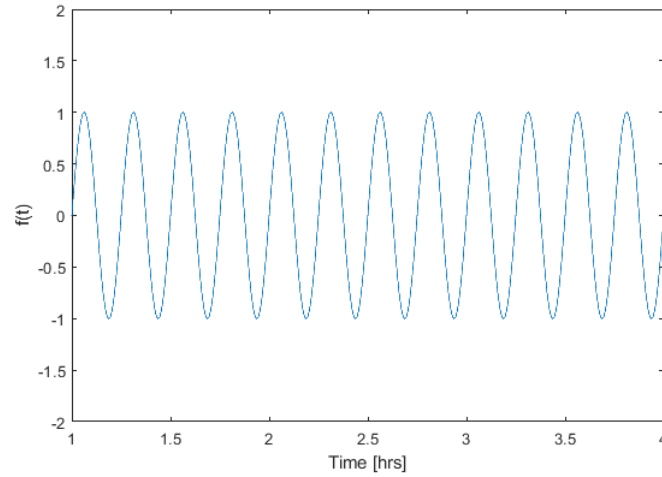


Fig. 3.8: Function  $f = \sin(2\pi t/p)$ , where  $p = 15$  min.

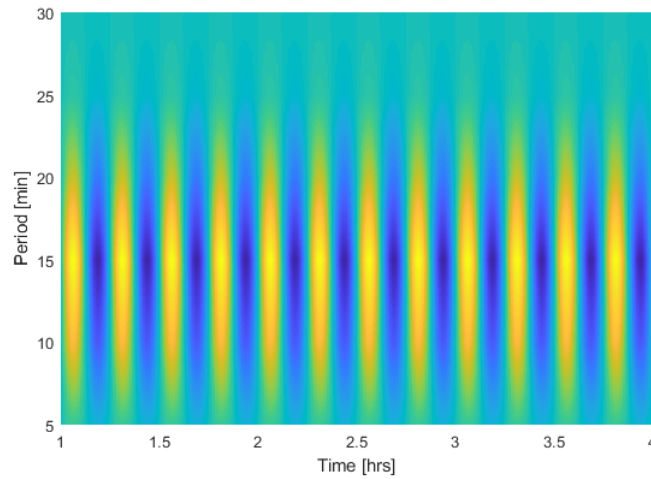


Fig. 3.9: Contour plot of CWT for the function  $f = \sin(2\pi t/p)$  using Mexican Hat wavelet. Default scale is used where blue corresponds to transform minima and yellow to maxima.

Values of  $T(a, b)$  are almost zero in the plot at both large and small values of  $a$ , but at intermediate values of  $a$  undulations in  $T(a, b)$  with period corresponding to the sinusoidal form of the signal are clear.

### 3.3 Discrete wavelet transform

In the CWT calculation, most information related to close frequencies or times are redundant and this operation requires a very high computational cost. In order to overcome these issues, the wavelet transform can be computed at discrete values of the dilation and translation parameters, and this procedure is called Discrete Wavelet Transform (DWT) [14].

To formally define the DWT, firstly it is necessary to discretize the wavelet of equation 3.8 as

$$\psi_{m,n}(t) = \frac{1}{a_0^{m/2}} \psi\left(\frac{t - nb_0 a_0^m}{a_0^m}\right), \quad (3.10)$$

in which  $a_0 > 1$  and  $b_0 > 0$  are fixed dilation and location parameter, and  $m, n \in \mathbb{Z}$ . Note that there is a link between the discretization of scales and locations, indeed the translation steps are proportional to the wavelet scale, i.e.  $\delta b = b_0 a_0^m$ . Probably the most employed choices for discrete wavelet parameters is the *dyadic grid arrangement*, namely  $a_0 = 2$  and  $b_0 = 1$

$$\psi_{m,n}(t) = \frac{1}{2^{m/2}} \psi\left(\frac{t - n2^m}{2^m}\right), \quad (3.11)$$

and DWT *detail* coefficients for a signal  $f(t)$  are

$$T_{m,n} = \int_{-\infty}^{+\infty} f(t) \psi_{m,n}^*(t) dt. \quad (3.12)$$

As a property of the wavelet analysis, it is possible to demonstrate that the amplitude of the wavelet coefficients is connected with abrupt signal variations of higher frequency.

Usually these wavelets are chosen to form an orthonormal basis in  $L^2(\mathbb{R})$ ,

$$\int_{-\infty}^{+\infty} \psi_{m,n}(t) \psi_{m',n'}(t) dt = \delta_{mm'} \delta_{nn'} \quad (3.13)$$

so that this setup is efficient for practical purposes because it removes redundancy in reconstructing the signal, since the information stored in a wavelet coefficient is never repeated. Explicitly, the reconstruction of a signal  $f(t)$  is computed by the *inverse* DWT:

$$f(t) = \sum_{m=-\infty}^{m=\infty} \sum_{n=-\infty}^{n=\infty} T_{m,n} \psi_{m,n}(t). \quad (3.14)$$

Let's now define the functions

$$\phi_{m,n}(t) = \frac{1}{2^{m/2}} \phi\left(\frac{t - n2^m}{2^m}\right), \quad (3.15)$$

with the property

$$\int_{-\infty}^{+\infty} \phi_{0,0}(t) dt = 1. \quad (3.16)$$

The function  $\phi_{0,0}(t)$  and its dilations and translations  $\phi_{m,n}$ , labeled as *scaling functions*, are associated with the smoothing of a signal  $f$ . The scaling functions can be convolved with the signal to produce *approximation coefficients*:

$$S_{m,n} = \int_{-\infty}^{+\infty} f(t)\phi_{m,n}(t)dt \quad (3.17)$$

An approximation of the signal at scale  $m$  can be obtained with a linear combination of the scaling function with coefficients given by equation 3.17, i.e. a sum over discrete translations:

$$f_m(t) = \sum_{n=-\infty}^{n=\infty} S_{m,n}\phi_{m,n}(t) \quad (3.18)$$

Now, let's designate the *detail space*

$$W_m = \text{span}_n\{\psi_{m,n}(t)\} \quad (3.19)$$

so that

$$L^2(\mathbb{R}) = \dots \oplus W_{-1} \oplus W_0 \oplus W_1 \oplus \dots, \quad (3.20)$$

and the *approximation space*  $V_n$ , generated by the scaling functions and satisfying the inclusion property

$$\dots V_2 \subset V_1 \subset V_0 \subset V_{-1} \subset V_{-2} \dots \quad (3.21)$$

The connection between  $W$  and  $V$  is

$$V_{m-1} = V_m \oplus W_m. \quad (3.22)$$

Supposing that the signal  $f(t)$  is contained in an approximation space  $V_m$ , we can define both the projection  $f_m$  of  $f$  on  $V_{m+1}$  and the detail function  $f - f_m$  belonging to the detail space  $W_{m+1}$ . Then from  $f_m$  it is achievable to get the projection on  $V_{m+2}$  and the detail in space  $W_{m+2}$ , and so on. To rebuild the original signal the procedure is simple: starting from the projection on the coarsest approximation space and all the projections on computed detail spaces, add the components in detail spaces with all the degrees of resolution to the approximation. In other words, the signal  $f(t)$  is expressed as a combination of an approximation of itself at arbitrary scale index  $\bar{m}$ , summed to a succession of details from scale  $-\infty$  to  $\bar{m}$ :

$$f(t) = \sum_{n=-\infty}^{n=\infty} S_{\bar{m},n}\phi_{\bar{m},n}(t) + \sum_{m=-\infty}^{\bar{m}} \sum_{n=-\infty}^{n=\infty} T_{m,n}\psi_{m,n}(t). \quad (3.23)$$

In some cases it is possible to totally reconstruct a signal using infinite summations of discrete wavelet coefficients (instead of continuous integrals as in the CWT). It is possible to demonstrate [14] that a necessary and sufficient condition for an accurate reconstruction of the original signal is the following:

$$A\|f\|^2 \leq \sum_{m=-\infty}^{m=\infty} \sum_{n=-\infty}^{n=\infty} |T_{m,n}|^2 \leq B\|f\|^2 \quad (3.24)$$

where  $A$  and  $B$  are bound parameters connected to the chosen wavelet. Reconstructed signal differs from the original one by an error depending on the ratio  $B/A$ , and

an exact reconstruction verifies when this ratio approaches unity. Identifying the *signal detail* at scale  $m$  as

$$d_m(t) = \sum_{n=-\infty}^{n=\infty} T_{m,n} \psi_{m,n}(t) \quad (3.25)$$

and rewriting equation 3.23, it is straightforward to prove that

$$f_{m-1}(t) = f_m(t) + d_m(t). \quad (3.26)$$

Last equation meaning is what defines a *multiresolution representation*, and expressly states that adding the signal detail at an arbitrary scale to the approximation at that scale, leads to a signal approximation of increased resolution.

This was just a brief introduction to DWT and multiresolution representation, but the explanation will not go more in detail because it is not the procedure we employed for the present work. However, in the next section one family of orthogonal wavelet which is often used to compute the DWT will be shortly described among the others, they are known as *Daubechies wavelet* [14].

### 3.4 Some wavelet families

This section summarizes the features of some important wavelet families which, in principle, are all appropriate for the analysis relative to this work: Gaussian derivatives, Morlet, Mexican hat, Daubechies and Meyer. In characterizing a wavelet function, the factors which should be considered are:

- *Orthogonality or nonorthogonality.* In orthogonal wavelet analysis, the number of convolutions at each scale is proportional to the width of the wavelet basis at that scale. So the wavelet spectrum is formed by discrete "pieces" of wavelet power, giving the most compact representation of the signal. Conversely, a nonorthogonal analysis can be really redundant at large scales, because the wavelet spectrum at adjacent times is highly correlated, so the nonorthogonal transform is used for time series analysis, for which wavelet amplitude are expected to be slowly varying;
- *CWT or DWT.* The choice of an orthogonal basis implies the use of the discrete wavelet transform, while a nonorthogonal wavelet function can be used with both the discrete and the continuous wavelet transform;
- *Complex or real wavelet.* While a real wavelet provides only a single component and can be useful to individuate phenomena like peaks and discontinuities in a signal, a complex wavelet function can return information about both amplitude (real part) and phase (imaginary part) and it is a better choice for capturing oscillatory behaviors;
- *Width.* In practice, the width of a wavelet function is defined as the dimension of the region where wavelet assumes non-zero values. Usually the width (or the

half-width) is defined as a multiple of the scales  $a$  (inversely proportional to frequencies with proportionality factor depending on the wavelet family), and it is important because determines which frequency component of the signal is being analyzed;

- *Shape.* The wavelet function should reflect in a good approximation the type of features present in the signal. For example, if one is interested in studying signals with sharp jumps or steps, a wavelet with abrupt changes like Daubechies would be an optimal choice, while for smoothly varying time-series a more regular function like Mexican Hat would be adequate;
- *Simmetry.* Some wavelet families shows a symmetric behavior around their center, but others do not, so it is the nature of the signal which tells what is more convenient for the analysis.

What follows is a list of the aforementioned wavelet families with a schematic description of their characteristics.

### Gaussian, Mexican Hat and Morlet wavelets

These are wavelets which satisfy the only admissibility requests (Eq. 3.7), namely Gaussian derivatives, Mexican Hat and Morlet. For this group of wavelets an example of a possible application is presented. In particular, contour plots of CWT analysis performed on the continuous function  $x(t) = \sin(2.5t) + \sin(12.5t)$  are shown. This function, composed of two sinusoids with a ratio of 5 between the arguments (Fig. 3.10), has been chosen in order to make visible the CWT ability to detect different oscillatory components.

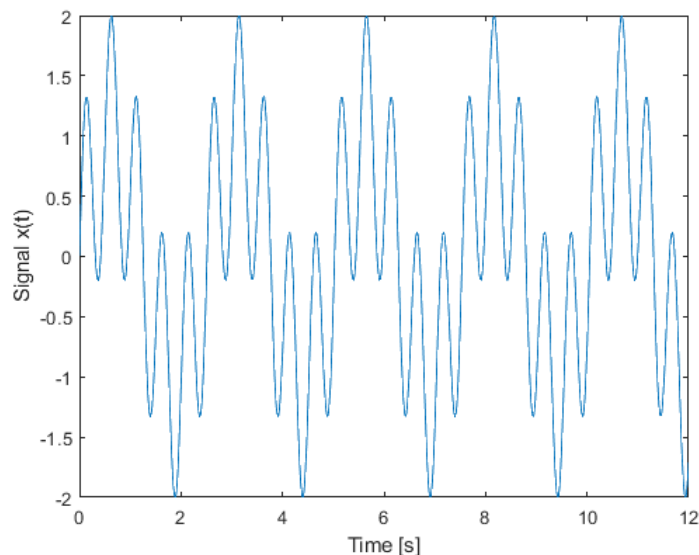


Fig. 3.10: Plot of function  $x(t) = \sin(2.5t) + \sin(12.5t)$ .

- **Gaussian derivatives.** The wavelet is defined as the Gaussian probability density function

$$\psi(x, n) = C_n \frac{d^n e^{-x^2}}{dx^n}, \tag{3.27}$$

where  $C_n$  is such that  $\|\psi(x, n)\| = 1$ .

Orthogonality	no
DWT	no
CWT	possible
Support width	infinite
Effective support	$[-4a \ 4a]$
Simmetry	n even $\rightarrow$ symmetric, n odd $\rightarrow$ anti-symmetry

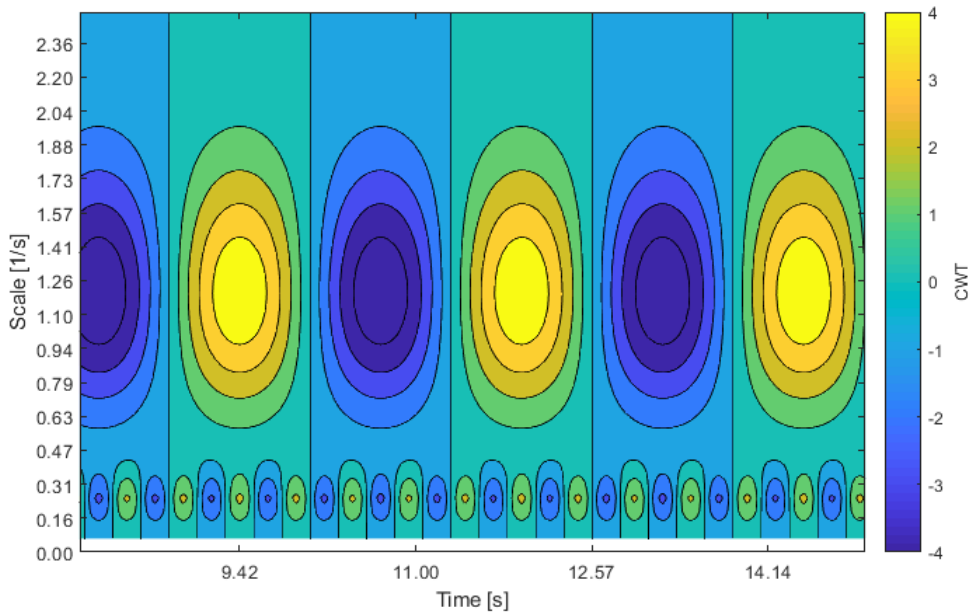


Fig. 3.11: Contour plot of CWT performed on  $x(t)$  with Gaussian 4<sup>th</sup> derivative wavelet. Scales  $a$  indicated on yaxis are connected with the signal frequencies  $f$  by  $f = \frac{1}{2a}$ .

- **Mexican hat** It is the second derivative of the Gaussian probability density function

$$\psi(x) = ce^{-x^2/2}(1 - x^2), \quad (3.28)$$

where  $c = 2/(\sqrt{3}\pi^{1/4})$ .

Orthogonality	no
DWT	no
CWT	possible
Support width	infinite
Effective support	$[-4a \ 4a]$
Symmetry	yes

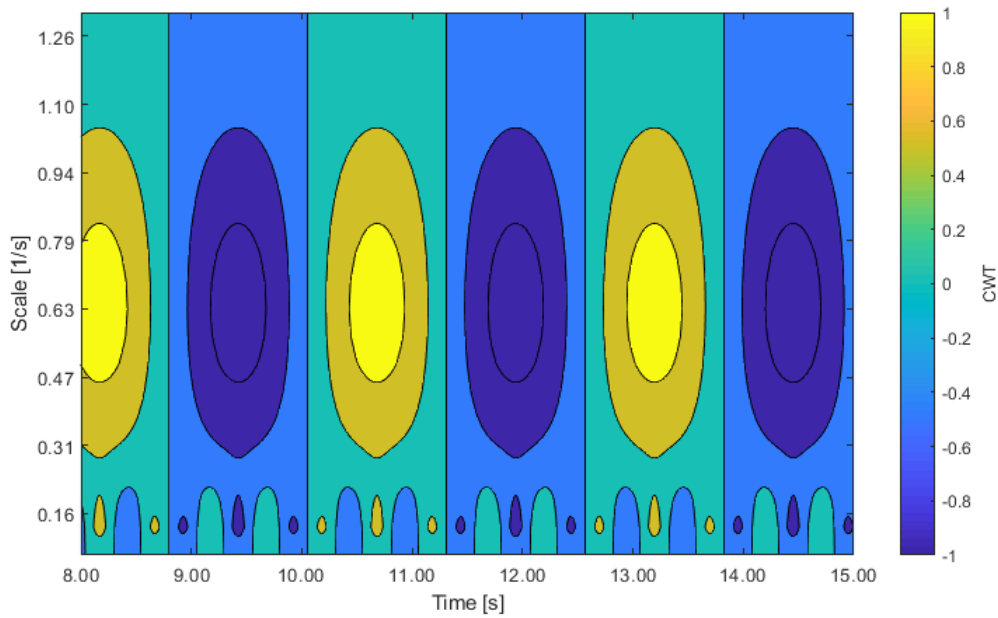


Fig. 3.12: Contour plot of CWT performed on  $x(t)$  with Mexican Hat wavelet. Scales  $a$  indicated on yaxis are connected with the signal frequencies  $f$  by  $f = \frac{1}{4a}$ .

- **Morlet** The definition is taken from equation 2.36 of [3]

$$\psi(x) = \pi^{-1/4} \left( e^{i2\pi f_0 t} - e^{-(2\pi f_0)^2/2} \right) e^{-t^2/2}, \quad (3.29)$$

where  $f_0$  is the central frequency of the mother wavelet.

Orthogonality	no
DWT	no
CWT	possible
Support width	infinite
Effective support	$[-4a \ 4a]$
Symmetry	yes

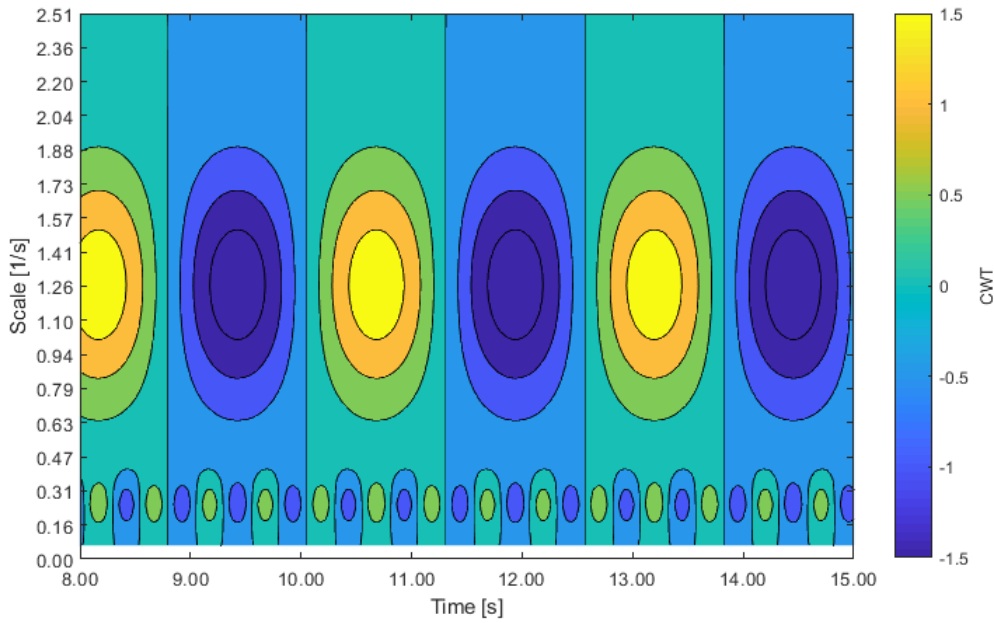


Fig. 3.13: Contour plot of CWT performed on  $x(t)$  with real part of Morlet wavelet of equation 3.29 where  $2\pi f_0 = 3$ . Scales  $a$  indicated on yaxis are connected with the signal frequencies  $f$  by  $f = \frac{1}{2a}$ .

Fig. 3.11, 3.12 and 3.13 result very similar. They all detect the two oscillatory components of  $x(t)$  accurately. The scales are linked to the two frequencies of the signal by the relations  $f_g = \frac{1}{2a}$ ,  $f_h = \frac{1}{4a}$  and  $f_m = \frac{1}{2a}$  respectively. However, some differences are present. For example, due to the analytic shape of Gaussian 4<sup>th</sup> derivative wavelet, Fig. 3.11 results in counter-phase compared to the other two plots. Additionally, wavelet transform coefficients appear comparable in Fig. 3.12 and 3.13, while in Fig. 3.11 they are larger (in absolute value).

## Daubechies

Daubechies- $n$  are compactly supported wavelets with  $n$  vanishing moments for a given support width (The  $n$ -th moment of a function is equal to the  $n$ -th derivative of its Fourier transform at zero frequency).

Orthogonal	yes
DWT	possible
CWT	possible
Support width	$2n-1$
Symmetry	no

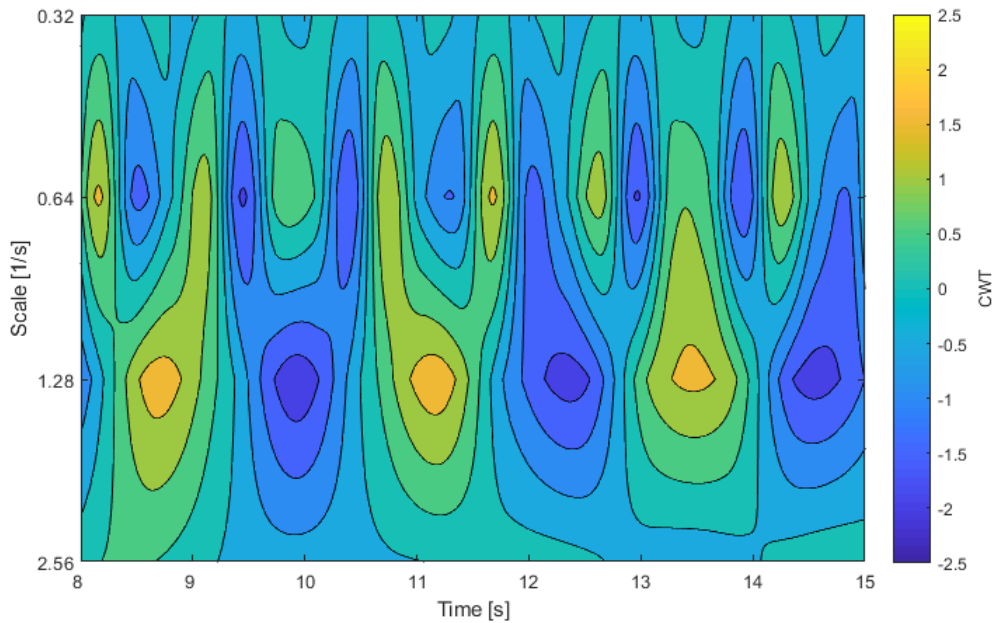


Fig. 3.14: Contour plot of DWT performed on  $x(t)$  with Daubechies4 wavelet.

Fig. 3.14 represents the DWT computation on signal  $x(t)$  by using Daubechies4 wavelet. It is immediate to notice that the ability in revealing the two sinusoidal elements is not as efficient as in the previous CWT calculations, in particular for the high frequency component.

### Meyer

It is an infinitely regular orthogonal wavelet, defined as

$$\psi(t) = \begin{cases} \frac{1}{\sqrt{2\pi}} \sin\left(\frac{\pi}{2}\nu\left(\frac{3|x|}{2\pi} - 1\right)\right) e^{ix/2} & \text{if } 2\pi/3 < |x| < 4\pi/3, \\ \frac{1}{\sqrt{2\pi}} \cos\left(\frac{\pi}{2}\nu\left(\frac{3|x|}{2\pi} - 1\right)\right) e^{ix/2} & \text{if } 4\pi/3 < |x| < 8\pi/3, \\ 0 & \text{otherwise.} \end{cases}$$

where

$$\nu(t) = \begin{cases} 0 & \text{if } x > 0, \\ x & \text{if } 0 < x < 1, \\ 1 & \text{if } x > 1 \end{cases}$$

Orthogonal	yes
DWT	possible
CWT	possible
Support width	infinite
Effective support	$[-4a \ 4a]$
Symmetry	yes

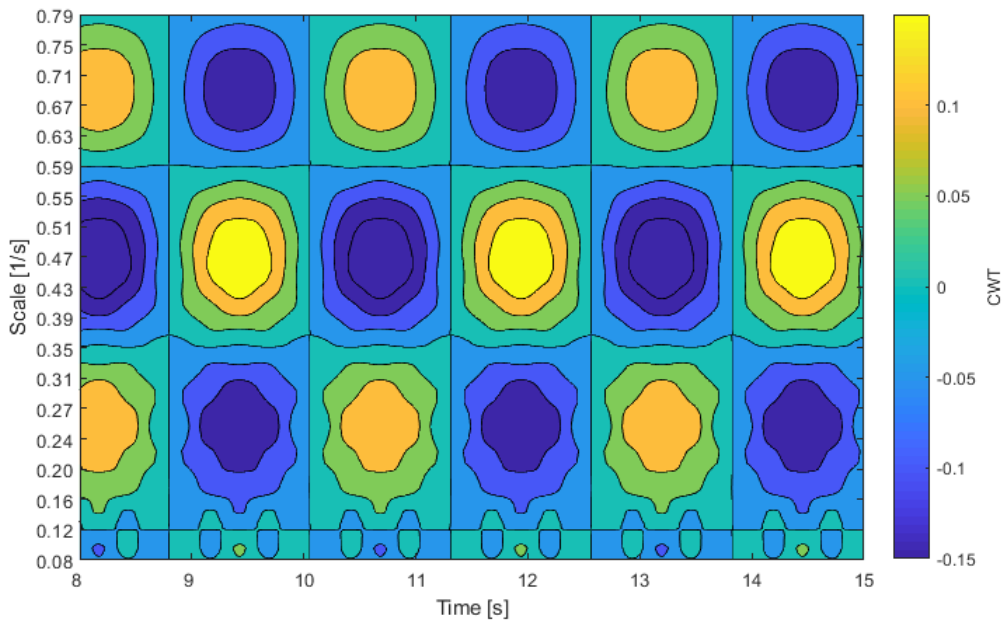


Fig. 3.15: Contour plot of CWT performed on  $x(t)$  with Meyer wavelet. Scales  $a$  indicated on yaxis are connected with the signal frequencies  $f$  by  $f = \frac{1}{4a}$

In Fig. 3.15 the two oscillatory components of  $x(t)$  are detected by the coefficients maxima (and minima) at scales connected with the frequencies of the signal by  $f_y = \frac{1}{4a}$ . Nonetheless, due to the piecewise definition of Meyer wavelet, the plot seems very different from the ones of Fig. 3.12, indeed the contour levels result split in several parts. Moreover, the higher frequency effects also higher scale here, while for previous cases a clear separation of the two scales were established. Finally, the wavelet transform coefficients assume values which are one order of magnitude smaller than for the Mexican Hat wavelet.

In chapter 4, these wavelet families will be tested on a subset of Materhorn experiment data, in order to identify the most suitable one for carrying out the complete analysis.

### 3.5 Wavelet analysis of complex terrain flows

Wavelet method has found numerous application in atmospheric science. In particular, in this section some example of works related to the study of boundary layer flows in which WT played a relevant role will be briefly presented first. Then, attention is focused on two research papers concerning wavelet analysis of complex terrain flows.

To start, one of the first works regarding the stable atmospheric boundary which exploited WT method is mentioned. Terradellas et al. [53] performed wavelet analysis on data recorded during the SABLES 98 field campaign [13] to investigate the atmospheric boundary layer under non-stationary conditions. They detected and characterized a wave-like wind event using a sum of some Morlet wavelets as model for the oscillation. Moreover, the phase differences in the wavelet transform were used to retrieve the wavelength and the phase speed of the oscillation. Then, they examined the behavior of small scale turbulence comparing the energy density per period and time unit with the wavelet transform modulus.

Rees et al. [43] focused the wavelet method on investigating a wave event in the stable atmospheric boundary layer overlying an Antarctic ice shelf. They performed orthogonal decomposition of velocity and temperature data by using the Daubechies10 wavelet, and then exploited the wavelet variance to assess the existence of a propagating internal wave and the presence of classical Gaussian noise, respectively connected to low and high frequency wavelet scales.

Recently, in [9] it was chosen to adopt the wavelet method in order to analyze nocturnal atmospheric surface-layer processes and surface-layer turbulent characteristics associated with the low-level jet during the Indian summer monsoon. Specifically, here wavelet allowed to separate the energy contributions in the frequency bands of a set of a time series of wind components measured by a lidar, with the aim of analyzing interactions among different scales of turbulent motion.

Cava et al. were active in research about nocturnal boundary layer over complex terrain by using WT, with a focus on the interaction with submeso motions. In [12], CWT based on the Morlet mother wavelet was exploited to characterize the timescale of the wavelike oscillations related to the coexistence of horizontal wind meandering and vertical submeso oscillations in wind speed and temperature time-

series collected during the Urban Turbulence Project [38]. Additionally, the wavelet cross-spectra were used to reveal the the common variability in frequency and time of different signals connected to the presence of gravity waves. A similar approach was followed in [37], where wavelet analysis was combined with Eulerian auto-correlation functions to study the coexistence of wave-like submeso motions and anisotropic intermittent turbulence in data measured at Espirito Santo State, Brazil [2].

After these short summary, it is important to mention two works wich are strictly connected with this thesis project. The first one is [44], which deals with the analysis of a stable boundary layer during the Boundary Layer Late Afternoon and Sunset Turbulence (BLLAST) field campaign. Data collected during this campaign indicated the existence of downslope flows generated at different locations after the evening transition, which were broken by the arrival of a mountain-plain wind. The studies about these interactions were performed by using WT with Morlet mother wavelet, applied to surface pressure time series measured by three microbarometers in order to detect energy peaks. Intervals in which the energy increase remained almost constant for a specific range of periods suggested the presence of coherent structures. In particular, since the onset of downslope flows, characterized by sudden modifications in wind speed and direction, often generates wave-like oscillations resulting by vertical displacements of air parcels from their equilibrium position called gravity waves, these specific phenomena were analyzed.

Gravity waves are also the central topic of the second work, presented in [56], where WT analysis was used to identify them among other coherent structures for different boundary layer variables in data gathered in Stable Atmospheric Boundary Layer Experiment Spain 2006 (SABLES2006) field experiment. In detail, cross correlation in wavelet domain was employed, in order to provide a simultaneous estimation of wavelength, phase velocity and direction of propagation of structures detected for every specific analysis window.

# Chapter 4

## The experimental setup

### 4.1 The MATERHORN campaign

The Mountain Terrain Atmospheric Modeling and Observations (MATERHORN) Program [16] was a 6 years project (2011-2016) funded by the U.S. Department of Defense. It gathered the expertise of a multi-institutional and multinational team of researchers, mainly from the University of Notre Dame, the University of California, Berkeley, the Naval Postgraduate School, the University of Utah and the University of Virginia. The purpose of this project was to characterize surface conditions related to mountain winds, investigate the planetary boundary layer in complex-terrain, study surface exchange processes, and to investigate the interaction of flows across a wide range of space-time scales employing complementary research methodologies. The overall goal was to identify and overcome the constraints of current state-of-the-art mesoscale numerical models for mountain terrain weather prediction. The program consisted of four parts:

- *MATERHORN-M (modeling)* investigated predictability at the mesoscale and performed high-resolution simulations using new modeling and different terrain-representation methodologies;
- *MATERHORN-T (technology development)* dealt with the development of innovative techniques for meteorological observations;
- *MATERHORN-P (parameterization)* allowed to generate physics-based fundamental relationships for complex-terrain processes;
- *MATERHORN-X (experimental)* principally conducted field measurements at inexperienced spatio-temporal detail also exploiting newly developed instrumentation. Two major campaigns were conducted in Fall 2012 and Spring 2013.

The location of this field experiment was the Granite Mountain Atmospheric Sciences Testbed (GMAST) of the U.S. Army Dugway Proving Ground (DPG) in Utah, located approximately 140 km south-west of Salt Lake City in the southern of Tooele County and just north of Juab County (Fig. 4.1).



Fig. 4.1: Three-dimensional map of Granite Mountain and Dugway Valley.

GMAST was an intensely instrumented test bed for studying atmospheric processes within complex-terrain near the Granite Mountain. Since 2016 all data has been made available by NCAR/EOL, which has provided access to the MATERHORN-X Final Data Archive [1].

## 4.2 MATERHORN-X, September - October 2012

The present work is based on the measurements collected during the Fall campaign of *MATERHORN-X*. In particular, the period from September 28, 2012 to October 2, 2012 was studied, although only analysis of days 28 and 30 September has been reported in chapter 4 since they provided the most representative results. The autumn campaign was selected based on the climatology of the area, which suggested prevalence of quiescent, dry, fair weather periods (700 hPa wind speeds  $< 5$  m/s) in which circulation is driven by diurnal heating and cooling, conditions favorable to the development of slope flows. The investigated complex terrain, i.e. the Granite Mountain, is an isolated peak with a length of 11.8 km, a largest width of 6.1 km, and an elevation 0.84 km above the valley floor (which is 1.3 km above sea level). Instrumented towers were placed along the east-sided and the west-sided slopes of Granite Mountain, part of large ensembles of devices located respectively at Intensive Observing Sites on east slope (IOS-ES) and west slope (IOS-WS). Especially relevant for the present work are the four flux towers ES2, ES3, ES4, and ES5 which were installed along the east slope of Granite Mountain and separated each other by a length of about 600-700 m (Fig. 4.2 taken from [24]).

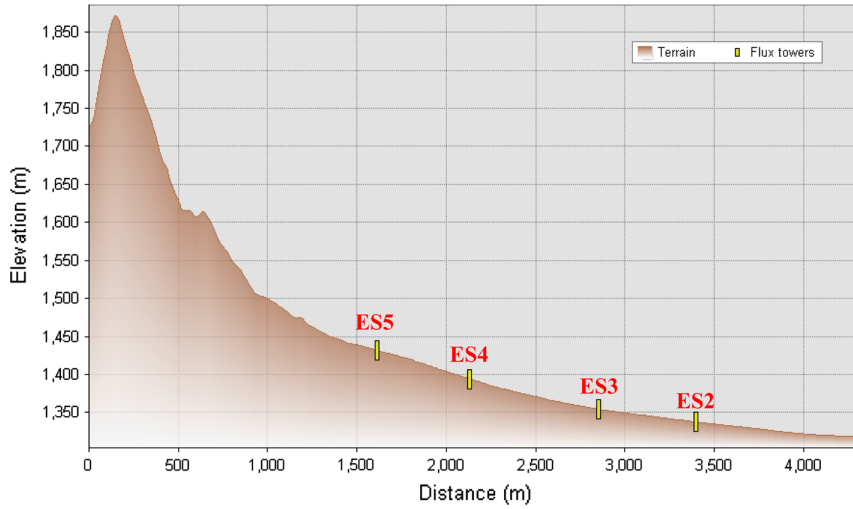


Fig. 4.2: Elevation cross-section at the location of the ES2-ES5 towers on the east slope of Granite Mountain. [24]

Information about the local topographical characteristics of the four towers (elevation, slope angle and slope azimuth angle), taken from [31], are listed in Table 4.1.

Tower	Elevation [m]	Slope angle [°]	Slope azimuth angle [°]
ES2	1338	1.6	95
ES3	1354	1.7	75
ES4	1394	5.8	104
ES5	1433	3.6	120

Table 4.1: Local topographical features of the four ES towers. Elevation is in meters above ground level (m AGL). The terrain inclination in the east-west direction gradually increases from ES2 to ES5 tower.

In each tower both high and low sampling frequency instruments were installed. In particular, every site was equipped with fast response three-axis sonic anemometers which sampled at 20 Hz wind velocity components (horizontal components  $u$ ,  $v$  and vertical component  $w$ ) and sonic temperatures. Slow response sensors designed to measure temperature (T) and relative humidity (RH) with sampling frequency equal to 1 Hz were placed on the ES2 and ES3 towers, and others with sampling frequency of 0.5 Hz on the ES4 and ES5.

For each tower measurements were gathered at several heights, varying from site to site but with a correspondence between fast and slow response devices. In detail, the sonic anemometers and the slow temperature/humidity instruments were located at seven levels on the ES2 tower (0.5, 4, 10, 16, 20, 25, and 28 m), at five levels on the ES3 tower (0.5, 2, 5, 10, and 20 m), at six levels on the ES4 tower (0.5, 2, 5, 10, 20, and 28 m), and at five levels on the ES5 tower (0.5, 2, 5, 10, and 20 m). This configuration allows for a detailed characterization of the flow structure and evolution near the ground, which is essential for shallow flows such as the downslope flows observed at this experiment site.

All levels of ES2 and ES4 were instrumented with *R.M. Young Model 81000* sonic anemometers, whilst the ES5 tower was equipped with *Campbell Scientific, Inc. CSAT3* sonic anemometers.

*Young* anemometer had the following characteristics:

- *resolution*: for wind speed 0.01 m/s, for wind direction 0.1°, for sonic T 0.01°C;
- *operating range*: for wind speed 0 to 40 m/s, for wind direction 0-359.9°, for sonic T from -50 to 50°C;
- *accuracy*: for wind speed  $\pm 1\%$  rms  $\pm 0.05$  m/s, for wind direction  $\pm 2^\circ$ , for sonic T from  $\pm 2^\circ\text{C}$ .

*CSAT3* anemometer had the following characteristics:

- *resolution*: for u and v is 1 mm/s rms, for w is 0.5 mm/s rms, for wind direction is 0.06 degrees rms, for sonic T is 0.025 °C;
- *operating range*: wind speed < 30 m/s, azimuth angles between  $\pm 170^\circ$ , sonic T from -30 to 50 °C;
- *accuracy*: for u and v offset error <  $\pm 8$  cm/s, for w offset error <  $\pm 4$  cm/s, for wind direction  $\pm 0.7^\circ$  at 1 m/s for horizontal wind.

The ES3 tower was an exception, since it was instrumented with a *Campbell CSAT3* sonic anemometer at the 2-m level and with *R.M. Young* sonic anemometers at other heights.

Slow frequency sensors at each tower were of the type *Vaisala HMP45*, whose characteristics are:

- *operating range*: for humidity 0.8-100% RH, for T from -40 to 60°C;
- *accuracy at 20°C*: for humidity  $\pm 1\%$  RH, for T from  $\pm 0.2^\circ\text{C}$ .

## 4.3 Data Pre-processing

The selection of the specific subset of MATERHORN data analyzed in this thesis will be described in chapter 4. The first step, before to proceed with the analysis, was to make a standard pre-processing of data, which involved essentially a despiking of data and a wind data rotation from the sonic coordinate system to Seemingly local earth coordinate (SLEC). These two process are described in the next sections.

### 4.3.1 Despiking

The despiking operation consists of detecting and eliminating short-term outranged values in the time series, which are due to instrument problems. The procedure here adopted follows [57]. Specifically, the procedure chosen for 20 Hz measured sonic data resided in removing spikes within a 1 minute moving average, with threshold equal to 3.5 times standard deviations for  $u$ ,  $v$  and sonic  $T$ , while equal to 5 times

standard deviations for  $w$  component. Sequences of four or more consecutive points detected as outliers were not considered as spikes. After having identified the spikes, they were replaced by a linear interpolation of surrounding values. For data collected by slow sensors despiking process was not necessary.

### 4.3.2 Wind data rotation

Air velocity measured by sonic anemometers is usually post-rotated from the instrument coordinate system to a reference coordinates suitable for objective analysis. Many rotation schemes are possible, and some of them are reported in [50]. One common choice is to use physical streamlines coordinates, so that the  $u$ -component is always parallel to the local mean velocity vector, while  $v_{mean} = w_{mean} = 0$  by definition [30]. Another option is to select a coordinate system which is fixed in space and time, therefore does not depend on the dynamic nature of the flow, e.g. Local earth coordinate (LEC) system, for which  $u$  is directed eastward,  $v$  northward and  $w$  parallel to local gravity. The rotation applied for the present analysis was into the Seemingly local earth coordinate (SLEC) system, which differs from the LEC one only by maintaining the same  $w$  as in sonic coordinates. As reported in [24], in the case of ES2-5 towers on the east-sided slope of Granite Mountain, the dissimilarity between LEC and SLEC was negligible. Indeed, the examined slope is a gentle slope, so it was correct to assume  $w$  as parallel to the local gravity vector making errors which were within the accuracy of experimental data.

As described in chapter 1, the main interest was to study the behavior of a downslope wind on the east side of the mountain, which has a main component blowing along-slope following an approximate West-East trajectory. As reported in Table 4.1, slope azimuth angles differed from the the east-west direction for few degrees, so it was a conceivable approximation for this study to consider the line connecting the four towers as parallel to this geographic orientation. Thus, in order to create a physical system where this major component was aligned to a particular axis, it was appropriate to rotate the coordinates into the SLEC system shown in Fig. 4.3.

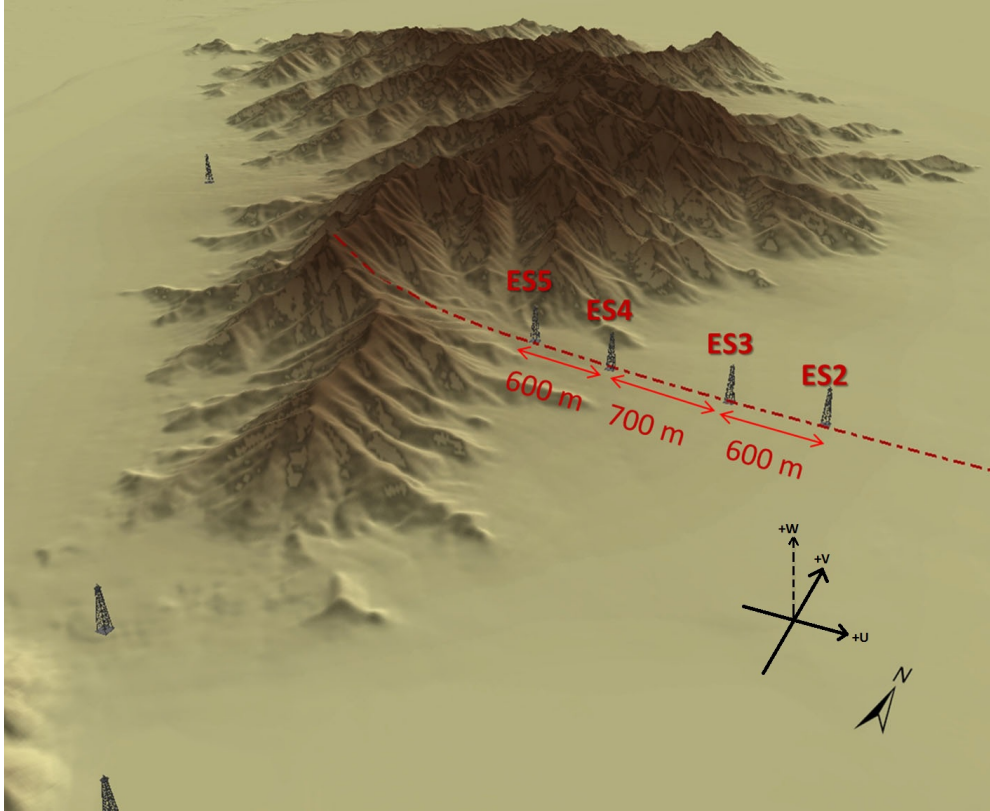


Fig. 4.3: Three-dimensional map with SLEC reference system. Adapted from [24].

*Young* sonic anemometer was oriented with  $v$  pointed to South and  $u$  pointed to West, while for *CSAT3*  $v$  pointed to East and  $u$  pointed to South, thus some manipulations were necessary to perform the rotation into SLEC system. In particular, the simplest manipulation is depicted in Fig. 4.4 and concerned the *R.M. Young* anemometers, so it was applied to ES2, ES3 except sonic at 2 m and ES4. The required operation was just to multiply by  $-1$  the instantaneous velocity component  $u$  and  $v$  vectors, i.e.  $u_{SLEC} = -u_{young}$  and  $v_{SLEC} = -v_{young}$ .

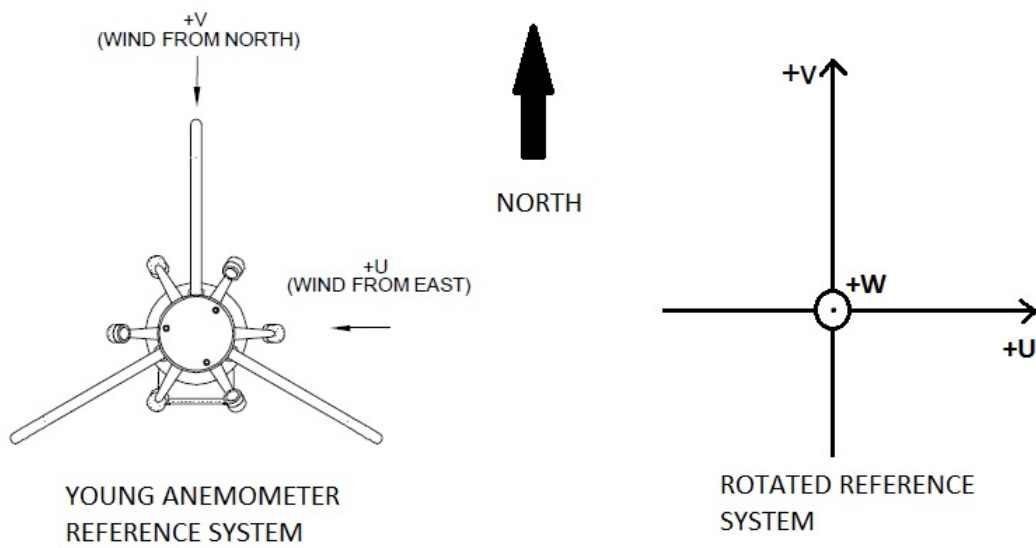


Fig. 4.4: On the left the Young anemometer reference system and on the right the rotated SLEC reference system.

*Campbell Scientific, Inc. CSAT3* anemometer relative to ES5 tower was established with a different orientation from the *R.M. Young* one, as illustrated in Fig. 4.5 and 4.6, and the link between these two instruments can be explicitly written as  $u_{young} = -v_{csat3}$  and  $v_{young} = u_{csat3}$ . Therefore, to rotate axis in the new reference system it was assumed  $u_{SLEC} = v_{csat3}$  and  $v_{SLEC} = -u_{csat3}$ .

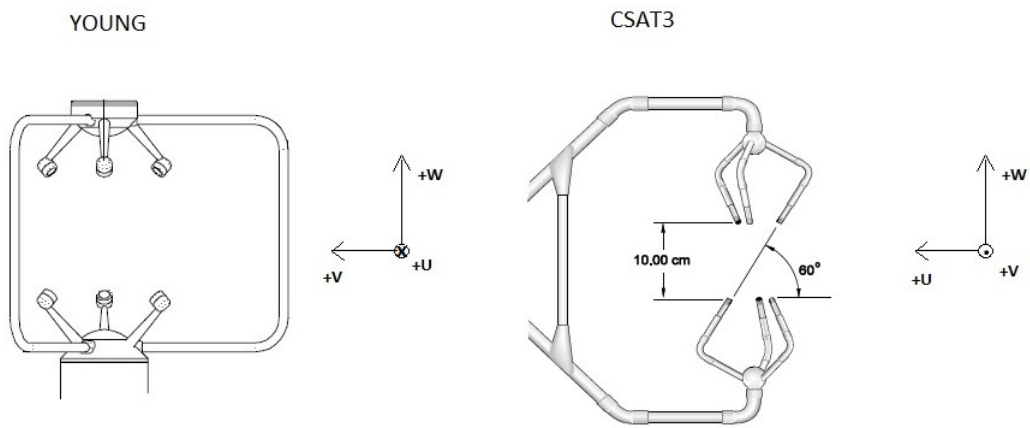


Fig. 4.5: *Young* and *CSAT3* anemometers orientation: side view.

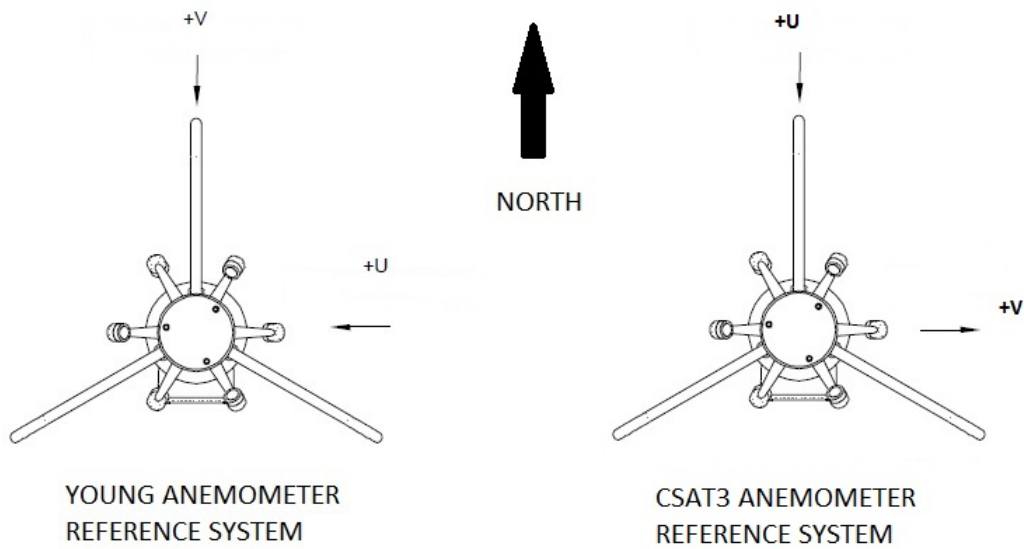


Fig. 4.6: *Young* and *CSAT3* anemometers orientation: top view.

Level 2 of ES3 data were measured by *Campbell Scientific, Inc.* *CSAT3* anemometer, pointed approximately to South-East as shown in Fig. 4.7, with exact angle relatively to true North equal to  $180 + 53 + 13 = 246^\circ$ , where  $13^\circ$  was the difference between true and magnetic North and  $53^\circ$  was the orientation of the sonic arm measured by magnetic compass directly on the ES3 site.

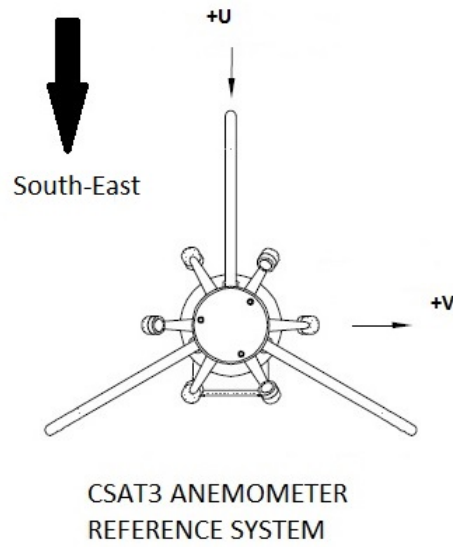


Fig. 4.7: *CSAT3* anemometer reference systems for ES3 at level 2.

In this case the rotation was realized in two steps, the first one transforming *CSAT3* anemometer coordinates into *Young* anemometer coordinates:

$$\begin{bmatrix} u_{young} \\ v_{young} \end{bmatrix} = \begin{bmatrix} \cos \theta & -\sin \theta \\ \sin \theta & \cos \theta \end{bmatrix} \begin{bmatrix} u_{csat3} \\ v_{csat3} \end{bmatrix} \quad (4.1)$$

where  $\theta = -156^\circ$ , and then rotating into SLEC reference system by using the same rotation of *Young* anemometer.

In the next chapter the experimental apparatus here described will be used for the analysis.

# Chapter 5

## Data analysis and results

In this chapter the analysis realized and the main results achieved are reported. The study was centered on the subset of MATERHORN 2012 experiment data described in chapter 3, which were investigated through the Wavelet Transform method. Regarding to this mathematical tool, it is necessary to say that the first idea was to exploit the Wavelet Toolbox which is part of the *MATLAB* numerical computing environment. Despite its undoubted efficiency and rapidity in producing ready-to-use results, this built-in tool was discarded due to its limited flexibility in the managing of the wavelet transform parameters, that would have constrained the analysis. Thus, it was opportune to create a code in *MATLAB* programming language, able to calculate CWT or DWT for wavelet families depicted in chapter 2, namely Gaussian 4<sup>th</sup> derivative, Mexican Hat, Morlet, Daubechies4 and Meyer. This program can work on any time-series of data, requiring as input parameters the scales and the locations where compute the transform, and provides the WT coefficients for the parameters and wavelet selected.

### 5.1 Selection of wavelet family

In order to select the most appropriate wavelet family to use for WT, initially a series of tests were performed. Daubechies4 was not taken into account because of the limits in the selection of scales which has to be in the form of  $2^{m/2}$ , as highlighted from Eq. 3.11. Meyer was also immediately discarded because its multidefined nature produced difficulties in the results interpretation, as seen in chapter 2, where it is reported that it was not able to clearly discern the two frequency in the sine function analyzed. For these reasons, the trial was restricted to a group of 3 wavelets: Gaussian 4<sup>th</sup> derivative, Mexican Hat and Morlet. CWT using these wavelets were computed for different variables, different measurement towers and anemometers. Here only the test referring to variable  $u$  measured by the anemometer of ES2 tower located at 4 m AGL from 2 to 4 UTC of Julian Day 272 (shown in Fig. 5.1) has been reported. The 2 hours long time span represented corresponds to interval 20-22 Local Time (during the analyzed period, Utah followed the Mountain Daylight Time (MDT), i.e. UTC -6).

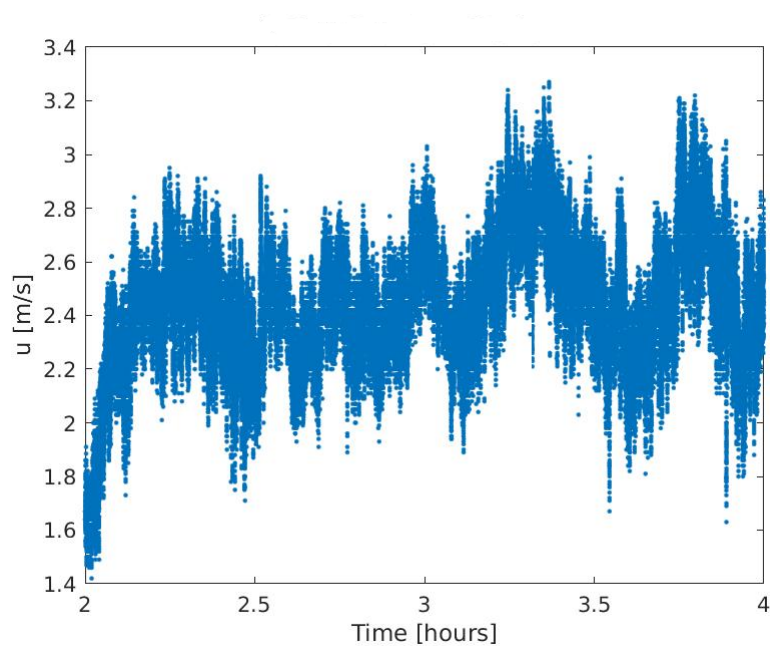


Fig. 5.1: Plot of  $u$  component measured by ES2 at 2 m from 2 to 4 UTC.

The following figures depict the contour plots resulting from CWT coefficient computation for the three different wavelet families, with analyzed periods (note that the wavelet period is defined equal to  $2a$ , or rather twice of the wavelet scale) ranging from 5 to 45 minutes. It is important to note that the wavelets used have a support spanning the interval  $[-4a \div 4a]$  (as reported in Sec. 3.4). Thus, in order to evaluate the CWT for a period of 45 minutes the data for the 90 minutes before and after the period analyzed are needed. During the study several tests have been performed to artificially extend the databases at the boundaries of the period analyzed (constant extension as done in [8], linear extrapolation, linear extrapolation added with turbulent fluctuations) with the purpose to overcome the limitations on the data availability and improve the computational performances. However, these tests showed that all methods strongly alter the CWT results.

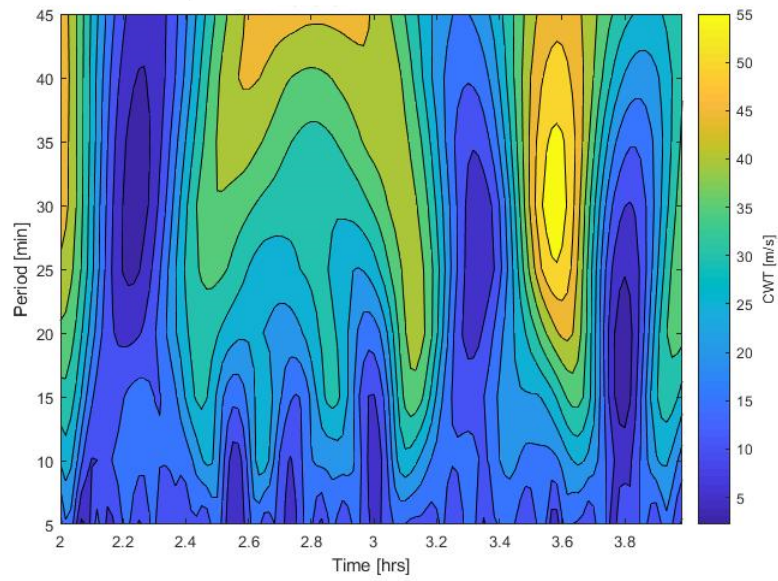


Fig. 5.2: Contour plot for  $u$  component of ES2 sonic 2 by using Gaussian  $4^{th}$  derivative wavelet.

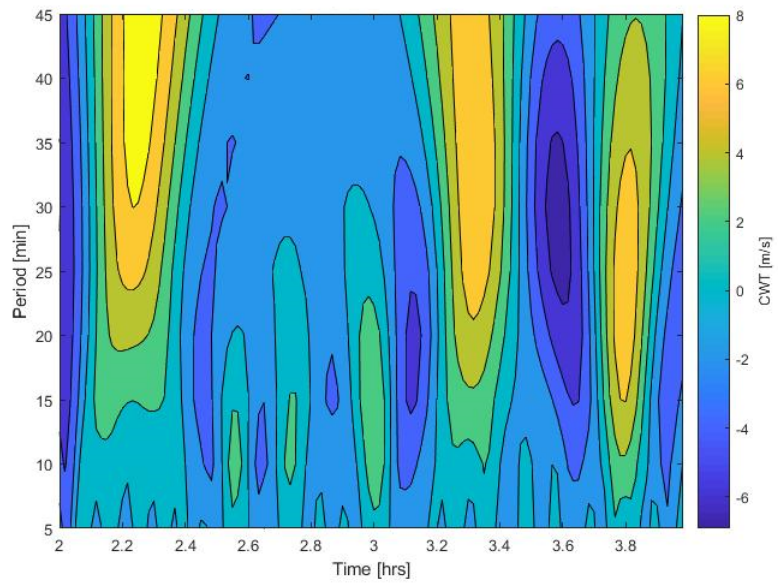


Fig. 5.3: Contour plot for  $u$  component of ES2 sonic 2 by using Mexican Hat wavelet.

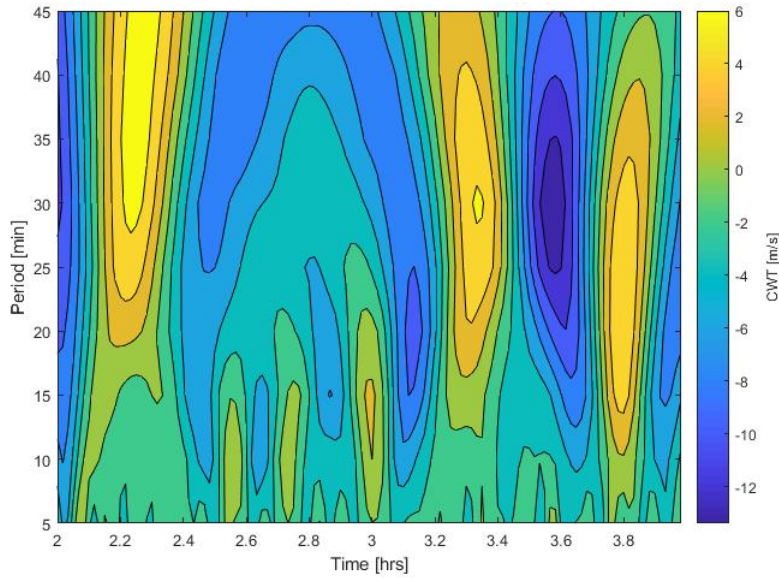


Fig. 5.4: Contour plot for  $u$  component of ES2 sonic 2 by using Morlet wavelet with  $2\pi f_0 = 3$ .

Observing the previous images, it is easy to notice some dissimilar features. In particular, Fig. 5.3 shows contours with a quite regular shape denoting the lower capability of the Mexican Hat in detecting phenomena in comparison with the Gaussian  $4^{th}$  derivative and the Morlet wavelets reported in Fig. 5.2 and 5.4, respectively. Looking at Fig. 5.2 and 5.4, besides the evident differences in values magnitude and the counter-phase behavior, no significant differences emerge. However, also contour plots regarding sonic temperature data were observed, and for this variable Morlet managed to depict separately the effects of the various scale phenomena, providing a better way in distinguishing the components of the signal than Gaussian  $4^{th}$  derivative. This more precise discrimination of the scales in temperature plots, added to the presence of other works performed with Morlet wavelet in literature to make comparisons with (e.g. [55], [56], [53]) contributed to decision of performing the study exploiting this kind of wavelet. Thus, all the analysis were made by using mother wavelet described by Eq. 3.29 with non-dimensional frequency  $2\pi f_0 = 3$ , which was chosen after checking that it provided correct results for known signals, as done in chapter 2 for the double sinusoid.

## 5.2 Selection of days and time intervals

After having selected the most appropriate wavelet for the analysis, choice about the dataset to study was made. This choice was mainly driven by other Materhorn studies reported in literature, in particular [24], [16] and [27]. As reported in Grachev et al [24], downslope flows were clearly observed in the early evening of Days 272-274-276. On the other hand, multiple types of flow interactions were discussed in Fernando et al. [16], and Hocut [27], sometimes leading to energetic collision with the downslope flow at the East Slope Site. The review of the literature

along with the preliminary inspection of the dataset in the pre-processing phase suggested Day 272 and 274 as suitable candidate for the in-depth Wavelet analysis presented in this thesis. The nighttime regime during those days indicates the presence of remarkably clear downslope periods followed by collision events and other interesting flow features. The selection of these days therefore allowed to investigate multiple flow regimes as well as the transition from one to another, and thus to fully exploit the capability of wavelet analysis to detect the nighttime characteristics and evolution of the flow at the East slope site. Fig. 5.5 and 5.6 represent for each of the aforementioned days the 5 minutes averaged wind directions in degrees from North for all anemometers of the four towers, which were utilized to detect the time range of interest. The main goal of this project was to use wavelet method to analyze the behavior of phenomena acting during nighttime flows and, since sunset occurred at 01:17 UTC whilst sunrise at 13:25 UTC, an initial large temporal domain was set from 0 to 14 UTC.

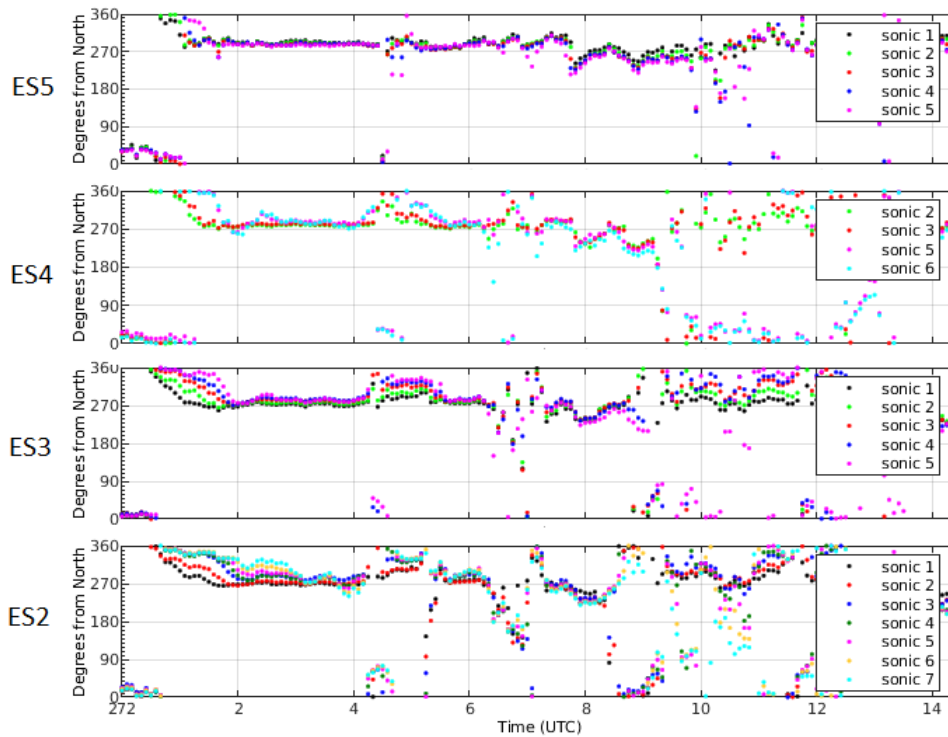


Fig. 5.5: All towers wind direction for day 272. ES4 data registered by sonic at level 1 (0.5 m), whose data were discarded due to a malfunction, are not shown. Even level 4 (10 m) of ES4 is not represented, because data were measured by sonic anemometer having opposite orientation during this day. This orientation was corrected later and those data were exploited for wavelet analysis.

From this figure it is possible to notice for day 272 a two hours long period from 2 to 4 UTC in which directions are aligned approximately in the downslope direction ( $270^\circ$  from North), in particular at towers located at high elevations such as ES5. This region seems well defined for every anemometer. The downslope regime appears significantly perturbed at about 5:30 UTC, but it appears to establish again until 6:30 UTC (especially for ES5). Thus, it was decided to analyze the period 0-8 UTC to catch all the potential concurring events.

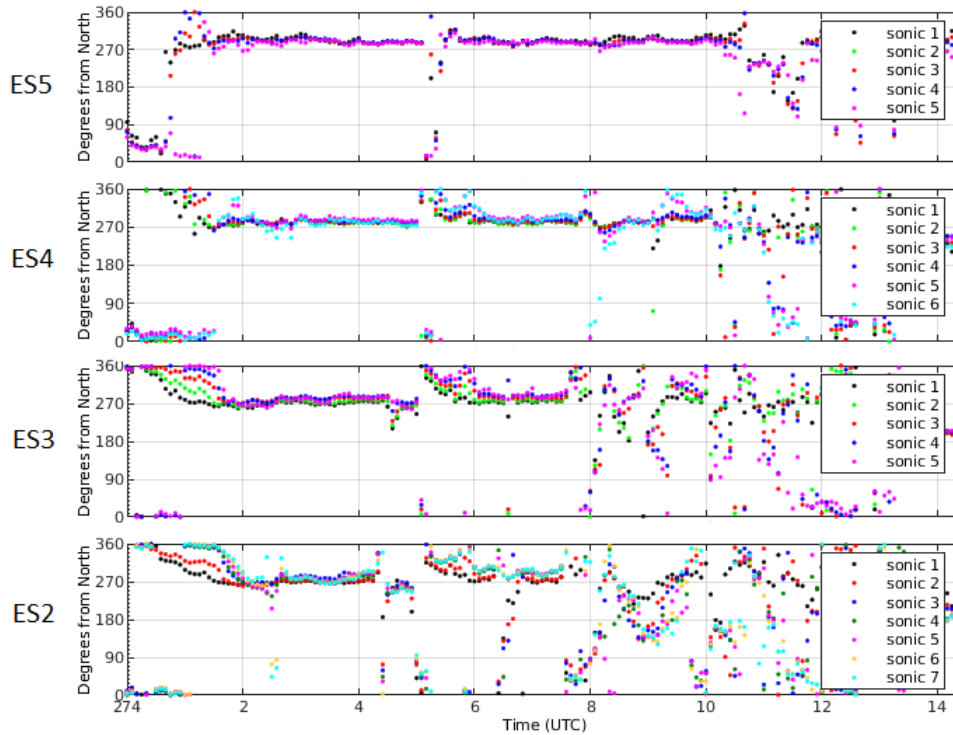


Fig. 5.6: All towers wind direction for day 274.

For day 274 the features are similar to day 272, with the eastward oriented flow from 2 UTC and until the disturbance occurring, in the interval 4-6 UTC. Then, the uni-directional flow is restored and lasts for several hours. However, in order to maintain a common time domain, also for this day the interval 0-8 was chosen as the range to study.

After the selection of days and hours objects of the investigation, it was necessary to determine accurately the range of periods at which downslope phenomena could theoretically occur, in order to have a fixed set of scales for the CWT computation. As described in [62], many works reported observations regarding oscillatory motions in downslope flows with periodicity between 5 and 90 minutes. The suggested inferior boundary was maintained during this study, also in agreement with the fact that events with period shorter than 5 minutes were in this case mainly linked to turbulence and not to wave-like oscillations. Instead, only in few cases it was decided to extend the analysis beyond 60 minutes period, because the temporal zone of interest rarely overcame 2 hours of duration, so it was not realistic to define as oscillatory phenomena the events with period longer than the domain. To summarize, the analysis were performed for Julian days 272 and 274 from 0 to 8 UTC, with CWT periods usually varying from 5 to 60 minutes, while  $b$  parameter moving with step equal to 5 minutes, a compromise between a number of data sufficient for the transform computation and a reasonable computational cost.

As mentioned in section 4.1 and described in depth in [3], when the wavelet approaches the limit of the data interval, a part of its support may fall out of the edge, producing a boundary effect. It consists of corruption of transform coefficients near to the boundary of the signal caused by lack of data to perform the computation of the integral in Eq. 3.9, since it requires the use of data outside the data interval considered in the analysis. Obviously, the affected area increases in extent proportionally to the growth of the parameter  $a$  of the analyzing wavelet. Reminding that Morlet wavelet support extends over four times the value of parameter  $a$  in each direction, and the connection between the period  $T$  and the scale is  $T = 2a$ , this means that, e.g., for  $T = 60$  minutes the CWT coefficients result affected for an interval of two hours from the boundary. In addition, the tests performed to evaluate the CWT with the artificial extension of the dataset showed strong limitations of these methodologies in mimic this unsteady and fluctuating data. For these reasons, in order to analyze aforementioned 0-8 UTC range it is required to extend the dataset of a time equal to  $2a$  at each boundary in order to complete the wavelet support.

### 5.3 28 September

The analysis of the nighttime flow evolution at the east slope site is here presented in detail for September 28. All three wind components  $u$ ,  $v$ ,  $w$  and the sonic temperature measured at 20 Hz, and the temperature registered by the slow frequency probes are investigated. To provide an initial overview of the wind behavior along the slope of the mountain, Fig. 5.7 is reported. It shows the wind direction for the four towers during the interval of interest at 10 m, an intermediate height which represents the bulk of the flow.

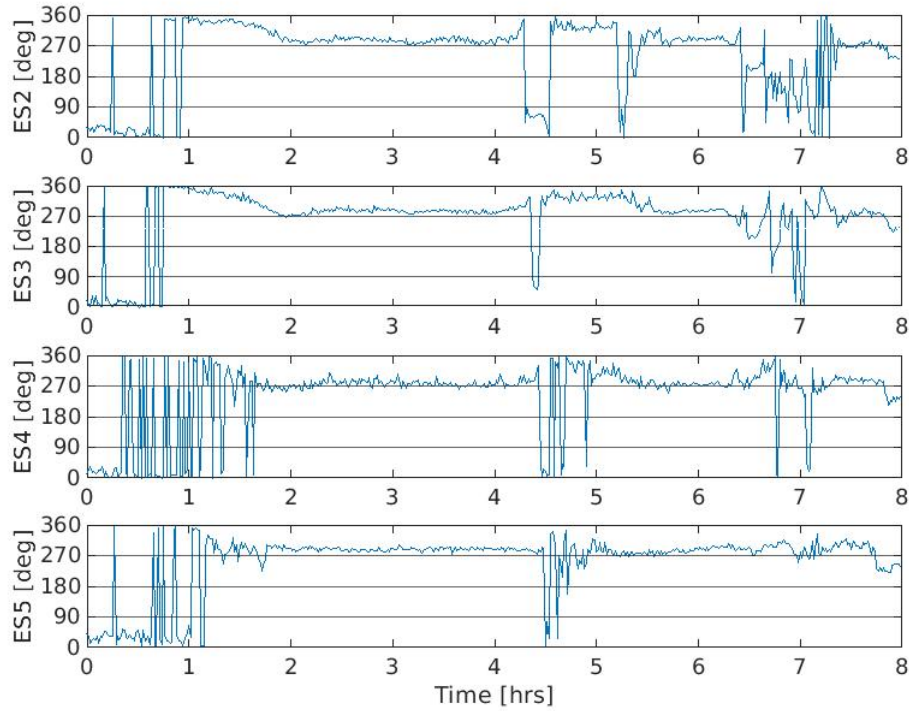


Fig. 5.7: Wind direction for day 272 for towers ES2-ES5.

Observing the figure, it is possible to distinguish three different flow regimes. The first one denotes the evening transition period, namely the transient regime preceding the onset of the downslope flow at approximately 2 UTC. The second is the "pure" *downslope regime* with a prevalent downslope wind direction towards East. This second interval encounters a perturbation approximately at 4:30 UTC, which determines the beginning of the third region. This last part of the signal dealing with this strong disturbance and what happens to the following perturbed flow which extends until the end of the dataset is named *collision region* for reasons that will be explained later. The three temporal areas will be discussed in the next sections.

### 5.3.1 Evening transition

The transient region was not the principal focus of the study, so the analysis did not go in depth. The main point of interest for this region is the behavior of the wind direction in the passage from a daytime flux to a katabatic nocturnal flow. Fig. 5.8 shows wind directions at 5 m for each tower from 0 to 4 UTC.

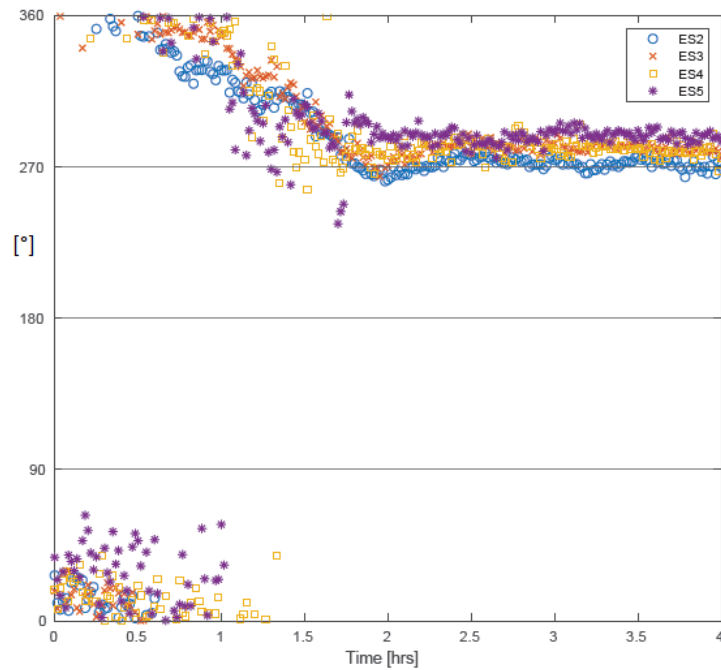


Fig. 5.8: Wind directions at 5 m.

It is possible to notice that directions align toward East gradually after 1 UTC (after sunset), and they stabilize approximately at 2 UTC. Indeed, this is the time at which the pure katabatic flow starts. Fig. 5.8 highlights that the change in direction first occurs at ES5 tower first, and then at other towers following the descent along the slope. This seems to be in agreement with the hypothesis of "stagnation front" cited in [17] and described in chapter 1, which states that downslope flow originates at the top of the slope and then propagates as a front down the slope.

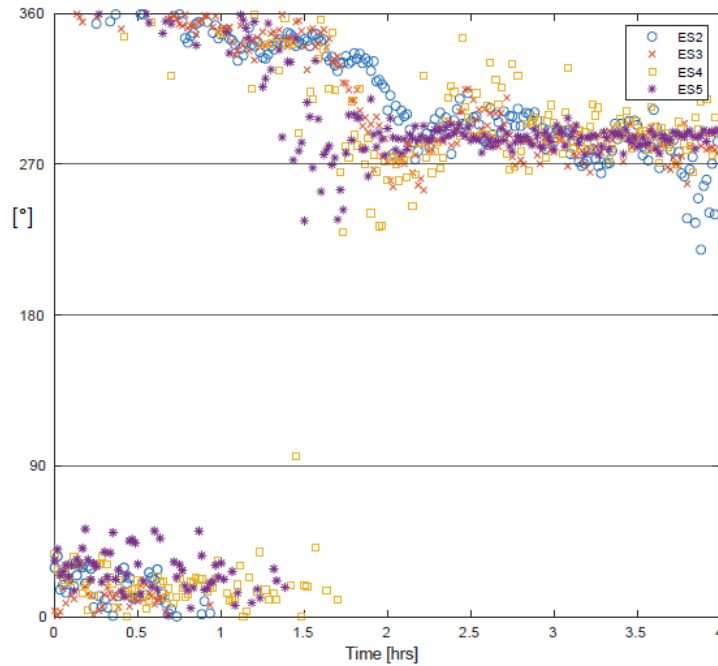


Fig. 5.9: Wind directions at 20 m.

Figure 5.9 depicts wind directions for each tower at 20 m. The behavior is similar to the one showed in the previous image, but the time alignment along East direction is not precisely defined. This reflects the fact that the downslope flow observed at Granite is relatively shallow, with a peak velocity registered at 2-5 m height. Therefore, the measurement level at 20 m might be more representative of the interfacial layer between the downslope flow and the ambient flow, especially while the downslope flow is not yet fully developed.

Figure 5.10 shows the data measured by sonic 4 (10 m) of tower ES5 in time interval going from 23:30 UTC of Julian day 271 to 3 UTC of Julian day 272 and shows from top to bottom: CWT contour plot for  $u$  component with period ranging from 5 to 45 minutes,  $u$  component time-series,  $v$  component time-series and wind direction.

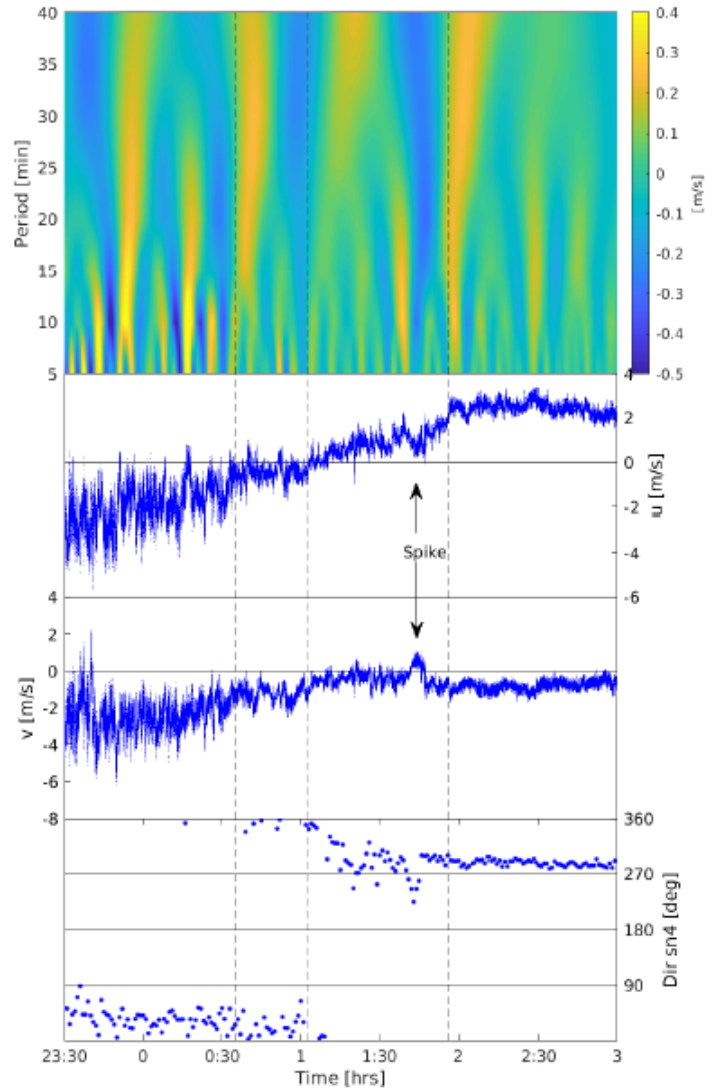


Fig. 5.10: CWT contour plot for  $u$  component with period ranging from 5 to 45 minutes,  $u$  component time-series,  $v$  component time-series and wind direction. All plots refer to ES5 tower, at 10 m measurement height.

Data from 23:30 to 00:30 highlight the passage from a regime with negative  $u$  and  $v$  and a prevalent South-West oriented direction to an eastward downslope wind with almost zero cross-slope component. Dashed lines divide the three sub-regions with distinct  $u$  behavior: from 0:30 to 1:00  $u$  has zero mean, from 1:00 to 2:00 it is positive and increases gradually, from 2:00 it stabilizes around 2 m/s. These variations of  $u$  are illustrated in the CWT plot as localized low frequency (period about 30-35 minutes) phenomena, which should not be intended as physically oscillatory motion having that period, but only a mathematical abstraction. Indeed, wavelet transform assigns values to the wavelet transform which allow to reconstruct the variable value with the inverse wavelet transform. In particular, the relatively high values for the transform at 00:30 associated with wavelet having long period are needed to reconstruct the transition from the regime where  $u$  is growing with the one where it is constant. Similarly, the negative values at 1:00 characterize the inverse transition.

Another phenomenon shown in Fig. 5.10 is a 10 minutes long spike occurring for  $u$  and  $v$  components before the beginning of the stable direction regime, and it is highlighted by the CWT with higher values involving all the frequencies. This particular event was found also in the anemometer located at 5 m, but at the moment a reasonable physical explanation has not been obtained.

### 5.3.2 Downslope regime

As anticipated before, the downslope regime starts approximately at 2 UTC where wind direction changes and align along a precise orientation. Fig. 5.11 and 5.12 show the wind velocity measured by every anemometer of all towers in a  $u-w$  plane, respectively at 00:00 UTC and at 02:00 UTC. Vertical axis represents anemometers height taking as zero ES2 tower base.

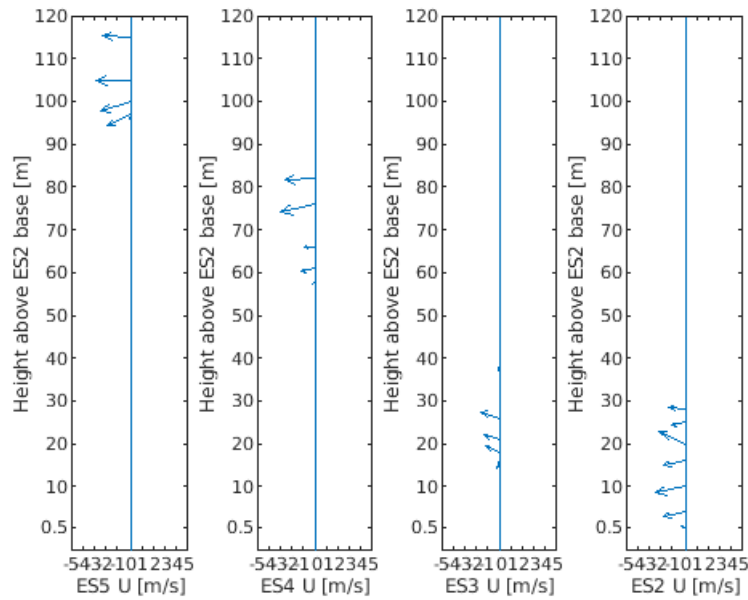


Fig. 5.11: Wind speed in  $u-w$  plane at 00:00 UTC.

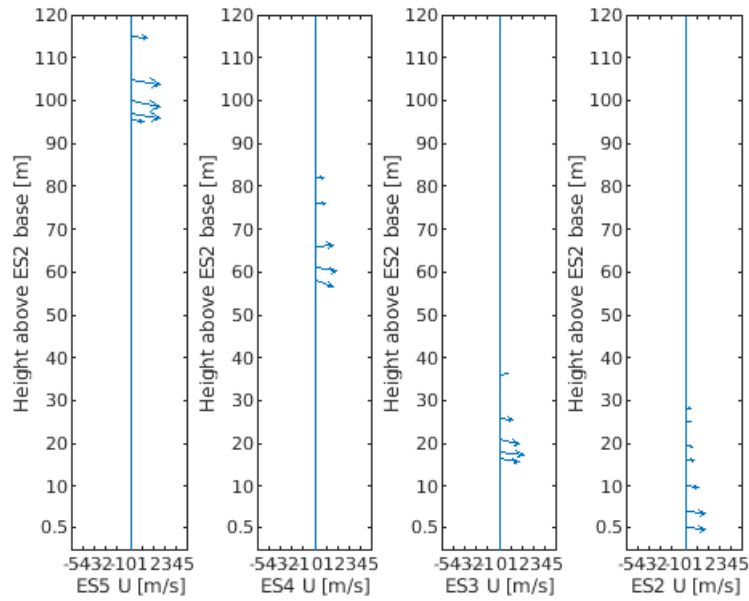


Fig. 5.12: Wind speed in  $u$ - $w$  plane at 02:00 UTC.

Observing these two images, it is immediate to notice the passage from an upslope  $u$  wind component which rises the mountain to a descending downslope flow. In Fig. 5.12, it is clearly shown the typical "nose" profile with wind maxima between 2 and 5 m from the slope surface. As further illustrated in Fig. 5.13, horizontal wind vectors at 5 m point in the same direction, which is close to eastward. Magnitude is considerable for ES5 and gradually diminishes going down the slope.

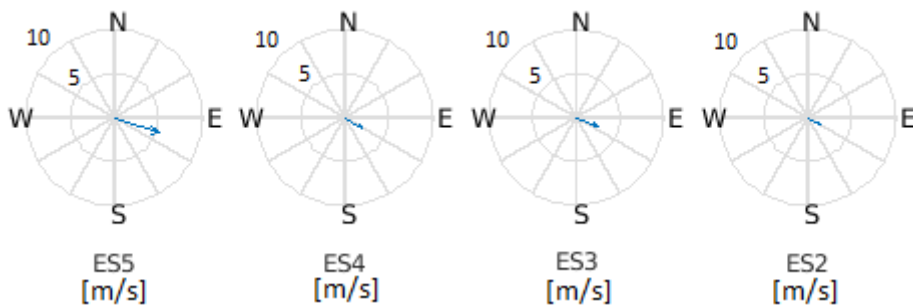


Fig. 5.13: Wind speed at 5 m in  $u$ - $v$  plane at 02:00 UTC. Every "slice" has angular opening equal to  $30^\circ$ .

After having established the existence of a katabatic flow, the focus was set in trying to extrapolate significant features. As reported in chapter 2, wave-like motions connected to katabatic flows have been theorized having period  $p = N \sin \alpha$ , where  $\alpha$  is the slope angle and  $N$  is the buoyancy frequency. In order to verify if these kind of oscillations are present in the examined downslope flow, firstly the evaluation of  $N$  was realized. Temperature data collected at each tower by the

vertical array of slow sensors allowed to estimate the temperature gradient at each tower, and therefore the computation of local  $N$ . This was initially accomplished by linear interpolation of temperature values registered at a fixed time by all sensors of each single tower, as shown in example of Fig. 5.14.

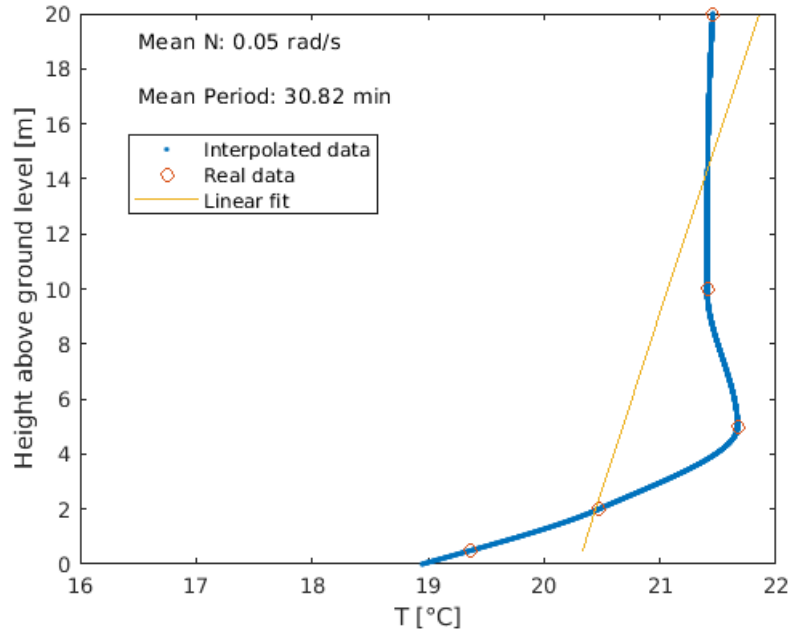


Fig. 5.14: ES5 temperature profile at 02:30 UTC. Interpolation realized considering all measures. Reported values of  $N$  and corresponding period are calculated averaging on the two hours interval (2-4 UTC) of downslope flow.

Instantaneous values of  $N$  were also averaged over the entire duration of the downslope regime, leading to a mean oscillation period of about 30 minutes for all towers, with small variations due to differences in temperature profiles and in slope angles at each site. Besides this overall estimation, the temporal trend and evolution of  $N$  was also estimated as shown Fig. 5.15. This was done by discriminating the lower, stably stratified layer of the flow, from the upper, weakly stratified part of it, and then estimating  $N$  in each portion. Such discrimination therefore allowed to take into account the drastic change observed along the temperature profile. More specifically, the lower layer, hereafter denoted as layer 1-3, extends up to third level of measurement (4 or 5 m depending on the tower) while the second layer is denoted as 3-5 and uses measurements from the upper sensors. Two different values for  $N$  were thus computed, one for each section, interpolating respective data as depicted in Fig. 5.15.

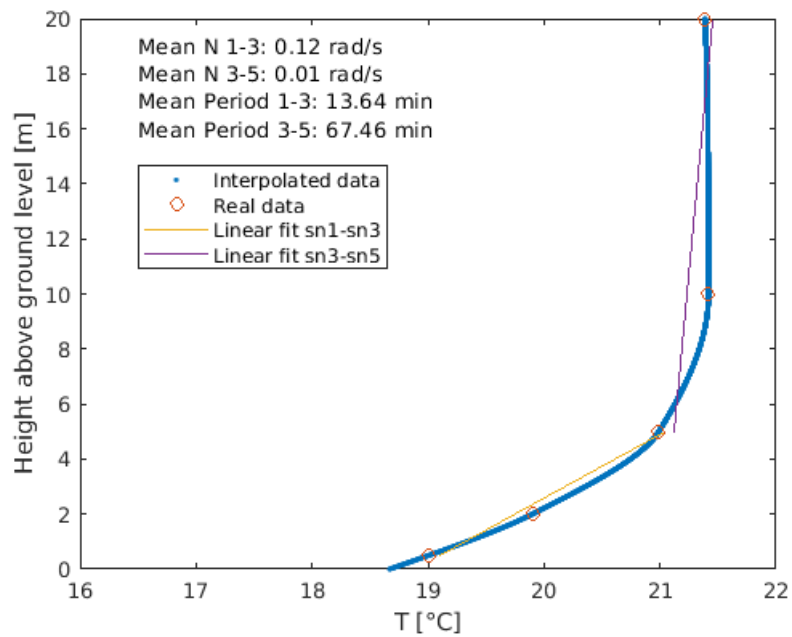


Fig. 5.15: ES5 temperature profile at 03:00 UTC. Double interpolation realized: from sensor 1 to 3, and from sensor 3 to 5. Reported values of  $N$  and corresponding period calculated averaging on the two hours interval (2-4 UTC) of downslope flow.

Values of the oscillation period calculated in the lower layer vary around 15 minutes, while in the upper zone periods are longer and near to 70 minutes. Fig. 5.16 represents the temporal evolution of  $N^2$  and corresponding period for each layer during the downslope regime at tower ES5.

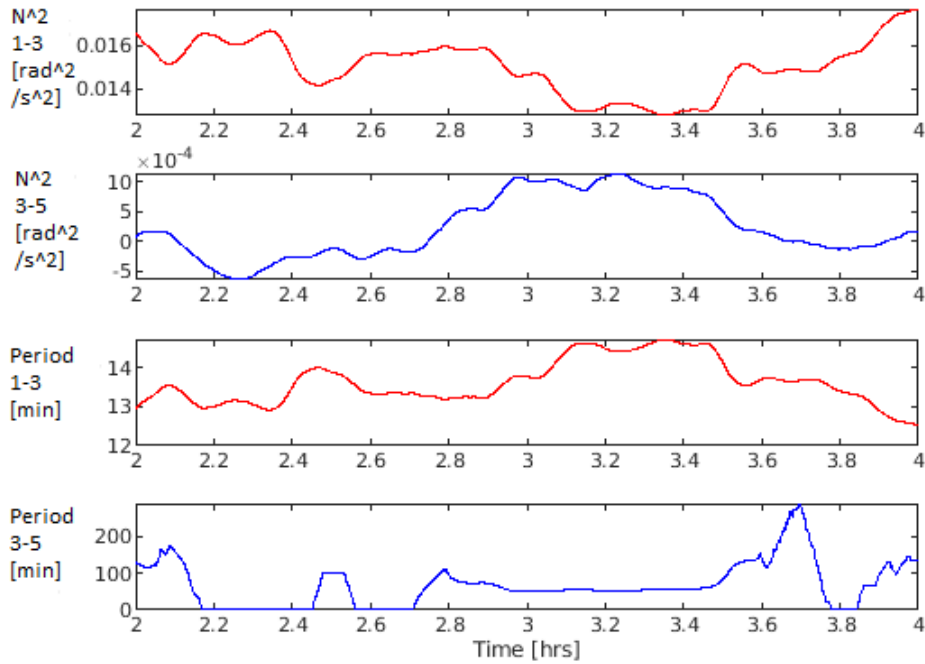


Fig. 5.16:  $N^2$  and corresponding periods during interval 2-4 UTC at tower ES5.  $N^2$  1-3 refers to the low layer, while  $N^2$  3-5 to the higher one. The same holds for periods.

It is possible to notice that period 1-3 slightly fluctuates between 13 and 14 minutes, while period 3-5 is approximately 60 minutes for major part of the interval, with some short ranges where it has no value since calculated  $N^2$  is negative. For other towers values of period in the low layer is similar, close to 15 minutes, while for the high layer period results greater, near 100 minutes. Since the theory predicts that downslope flow may exhibit oscillatory behavior having the computed periods, the goal was to search for these flow features through the wavelet analysis.

The quantity whose analysis provided the most interesting results was  $u$  wind component of ES5, because it was observed that katabatic flow firstly established at this tower. Figure 5.17 shows wavelet contour plot for  $u$  component at 2 m in interval 2-4 UTC along with the values of  $u$  and  $v$  components of velocity and the angle of between the velocity vector and the North direction.

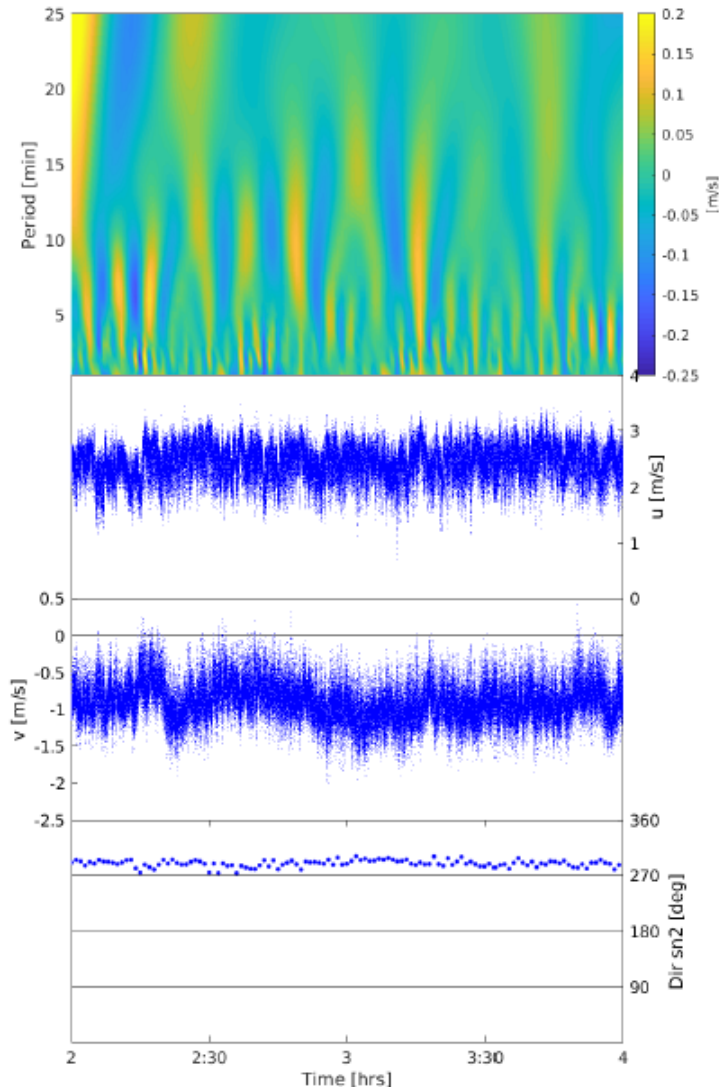


Fig. 5.17: CWT contour plot for  $u$  component at 2 m with period ranging from 5 to 25 minutes,  $u$  component time-series,  $v$  component time-series and wind direction.

In this case, wavelet analysis indicates the presence of an oscillatory component in the downslope flow, but only at higher frequencies. Specifically, wavelet coefficients reached maximum value of 0.1 m/s in correspondence of a period of about 8 min. The oscillatory component with  $p = 8$  min is present for most of the duration of the downslope regime, and gradually decays in magnitude after 3:30 UTC. This phenomenon was visible for all anemometer levels of ES5, as further detailed in Fig. 5.18 [Note that the minimum of the wavelet coefficients (0.05 m/s) detectable at 02:30 UTC in Fig. 5.17 does not represent a real decay in this oscillation magnitude, but it is a mathematical artifact due to the interference with a long period feature caused by the transition from transient flow regime to katabatic flow regime, as described in previous section].

Figure 5.18 provides the time evolution of wavelet coefficient having  $p = 8$  min for all anemometer installed in ES5.

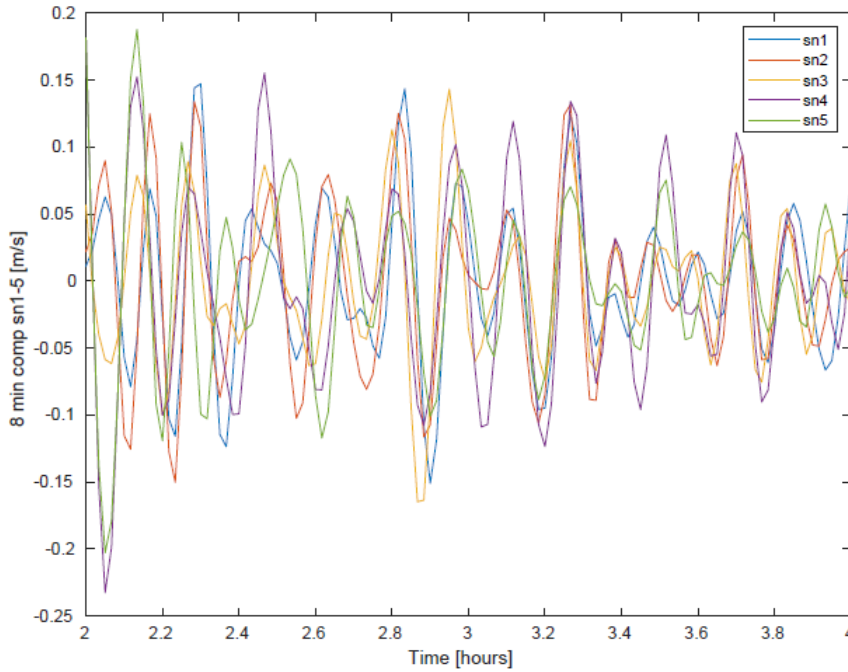


Fig. 5.18: Time evolution of CWT coefficient for  $u$  at ES5 relative to  $p = 8$  minutes.

It is easy to see a sinusoidal behavior of these coefficients for each anemometer, moving in phase after an initial adjustment interval. This suggested an oscillatory behavior involving the entire flow. In addition, greater values of these coefficients found for higher anemometers indicate that such oscillation intensified at the top of the flow. This aspect, along with the discrepancy between this period and the one estimated through the relationship  $p = 2\pi/(N \sin \alpha)$ , suggest that oscillations with  $p = 8$  min might not be of the type theorized in [18] and reported in [42], i.e. an intrinsic property of the downslope flow, but rather triggered by external factors. Presence of high frequency oscillation for  $u$  component was investigated also for the other instrumented towers. ES4 exhibited some similarities with ES5, indeed undulations at period close to 10 minutes were detected for top anemometers and for a shorter time range (2-3 UTC), while for towers positioned at low elevations this contribution was still present but less. Longer period oscillations ( $p = 20$  min) were found at ES3 and were remarkably visible at ES2. Fig. 5.19 shows wavelet plot for sonic 5 (20 m) of ES2, where the event is clearly evident.

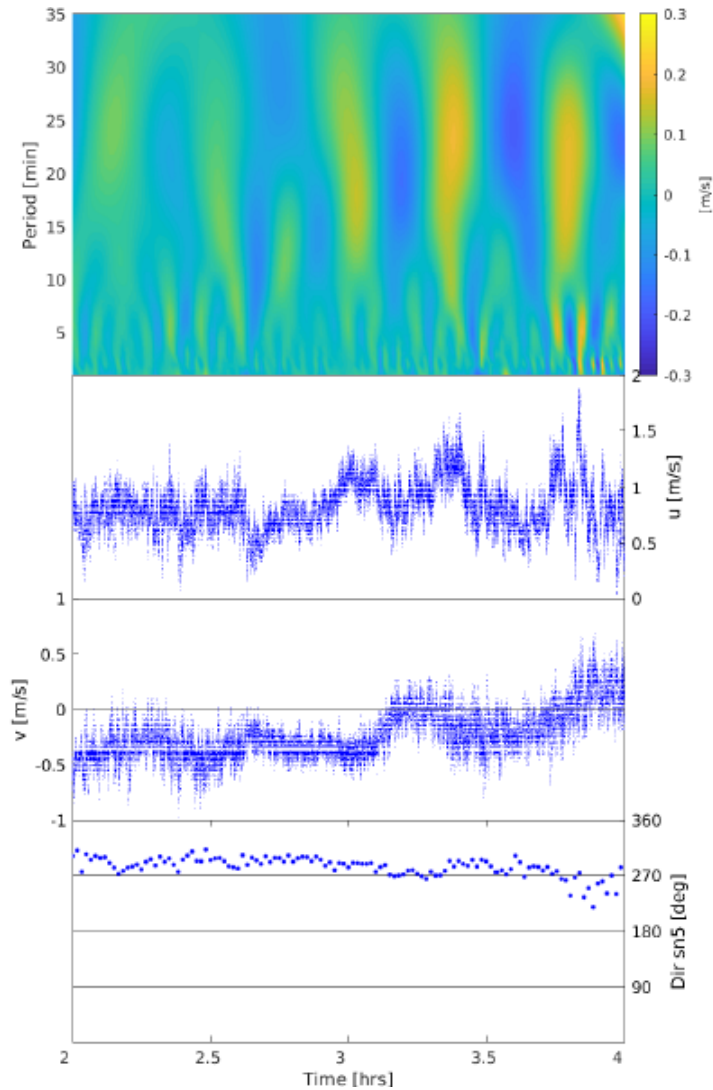


Fig. 5.19: CWT contour plot for  $u$  component with period ranging from 5 to 35 minutes,  $u$  component time-series,  $v$  component time-series and wind direction. Plot refers to sonic 5 (at 20 m) of ES2.

The 20 minutes period oscillation became considerable especially after 3 UTC, while the high frequency oscillations continue to be present. Fig. 5.20, similarly to Fig. 5.18, depicts time evolution of 20 minutes component.

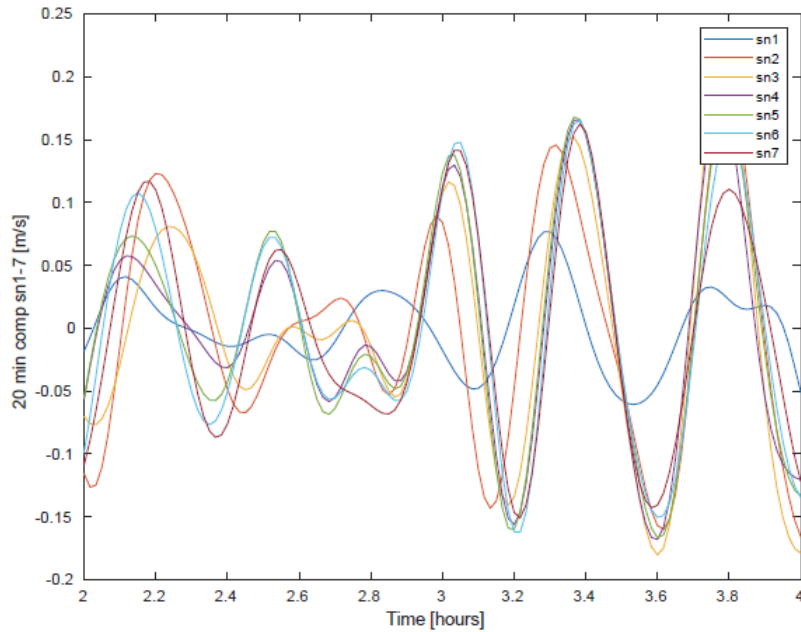


Fig. 5.20: Time evolution of CWT coefficient relative to  $p = 20$  minutes.

It makes more visible the substantial contribute of 20 minutes component particularly after 3:00 UTC. All levels are represented, and it is noticeable that the greatest values refer to the uppermost anemometers. Only instrument at level 1 seemed not to follow the common path, maybe appreciably affected by turbulent motions near the surface.

20 minutes periodic oscillation was thought the downslope to be the results of the interaction between the downslope flow and the valley wind circulation, rather than a property of the downslope flow itself. This hypothesis was suggested by the fact that intensity of this event was stronger for ES2, whose position was the closest to the valley, and by the fact that it disappeared in towers ES4 and ES5, i.e. away from the valley. In support of thesis which states that these undulations derived from valley circulation, it is important to mention that observations concerning oscillations with this typical 20 minutes period were reported in [41], in which they were attributed to pulsations of nighttime down valley wind current.

### 5.3.3 Collision region

Looking back at Fig. 5.7, a peculiar feature in wind direction evolution is distinctly visible. At 4:30 UTC, a powerful perturbation occurred, producing a remarkable fluctuation in wind direction. The disturb lasted for several minutes, with longer duration for ES2 than other towers. Moreover, it is possible to notice a time delay of the appearance of this occurrence among the group of towers. In particular, the perturbation firstly developed in ES2, and then propagated along the upslope direction, eventually reaching ES5. This characteristic allowed to theorize that this disturb was associated with the impact of an external wind coming from the

valley which surrounds the mountain with the already established downslope flow, as assessed in [27]. For this reason, this event was classified as a *collision* between two fronts. The collision hit ES2 at 4:19 UTC, and arrived at ES5 at 4:31 UTC, with a 12 minutes delay. Since the distance between the two towers is equal to 1900 m, this implies an upslope front velocity of 2.6 m/s, comparable to the values of  $u$  and  $v$  which characterize the flow after the collision. Indeed, the behavior of these two components can be understood observing the  $u-v$  plane plots of velocity vectors at 20 m in Fig. 5.21-5.24.

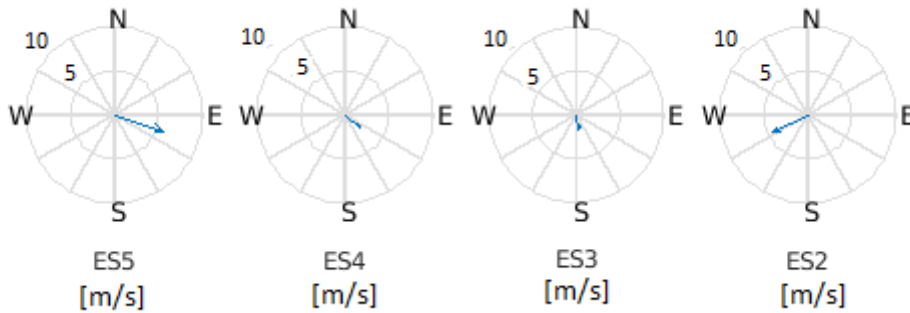


Fig. 5.21: Wind speed at 20 m in  $u-v$  plane at 04:20 UTC.

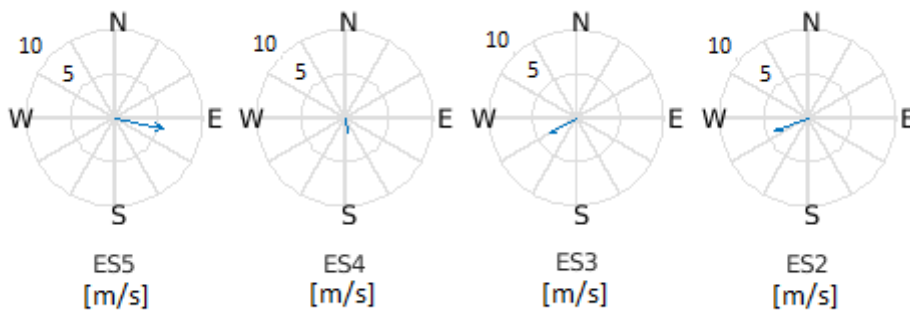


Fig. 5.22: Wind speed at 20 m in  $u-v$  plane at 04:25 UTC.

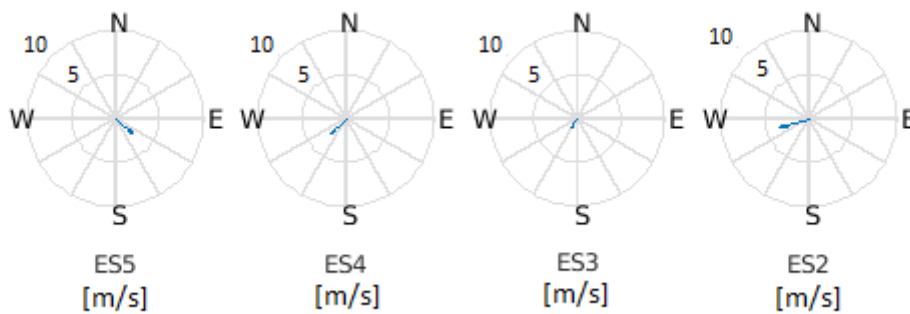


Fig. 5.23: Wind speed at 20 m in  $u-v$  plane at 04:30 UTC.

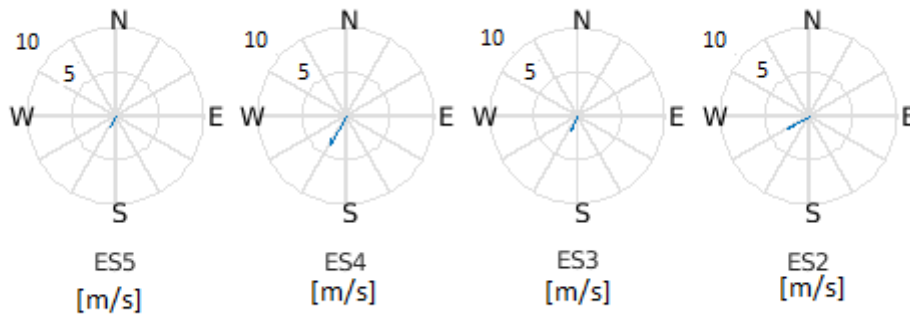


Fig. 5.24: Wind speed at 20 m in  $u-v$  plane at 04:35 UTC.

It is quite simple to distinguish the valley front arrival and its contact with the already existing downslope flow. Fig. 5.21 shows that at 04:20 the collision had already reached ES2 and the velocity reached a magnitude close to  $5\sim\text{m/s}$  and the direction  $120^\circ$  from North. At this time also ES3 was perturbed by the collision phenomenon, indeed the magnitude of velocity is small, while ES4 and ES5 still were characterized by the katabatic flow. At 4:25 (Fig. 5.22) also in ES3 was measured a larger velocity with  $120^\circ$  from North orientation, the collision front moved to ES4, while ES5 still registered downslope flow. Fig. 5.23 shows that at 4:30 the velocity in ES4 had the same alignment as in ES2 and ES3, and in ES5 had been perturbed from the previous regime.

This collision event was examined by using wavelet method, which also supplied information about resulting oscillatory phenomena. The following figure shows wavelet transform coefficients plot for tower ES5 at 5 m, a specific case chosen because collision had a short duration there and its features were well depicted.

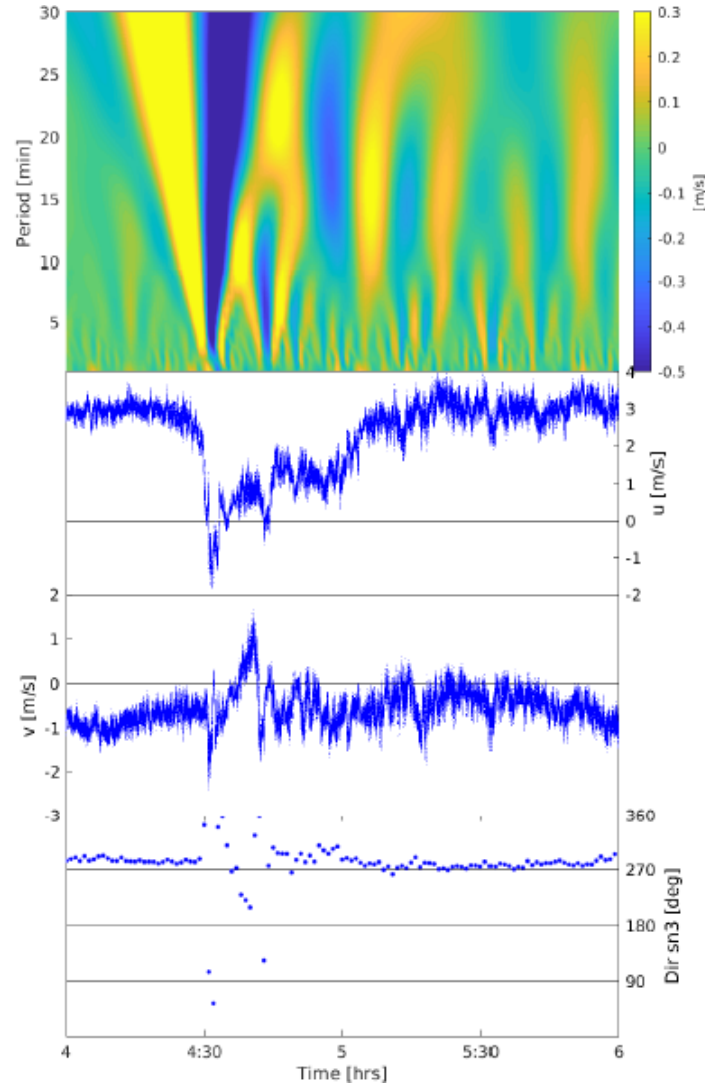


Fig. 5.25: CWT contour plot for  $u$  component with period ranging from 1 to 30 minutes,  $u$  component time-series,  $v$  component time-series and wind direction.

Collision is detectable through wavelet methods because a time-localized band of high intensity transform coefficients appeared at all frequencies. The collision is a strong change in velocity magnitude and direction, Fig. 5.25 shows that at 4:30 the velocity component  $u$  changed from about 3 to -2 m/s. This was followed by a long "tail" of a perturbed state with inner oscillations. From 4:30 to 5:30 the  $u$  component of the velocity increased until the katabatic flow regime was re-established. The increment of  $u$  was not monotonic, but it included oscillations that are highlighted by the CWT which provides information about their magnitude and period. Because of these characteristics, it needs of the contribution of all wavelet scales in order to be properly represented.

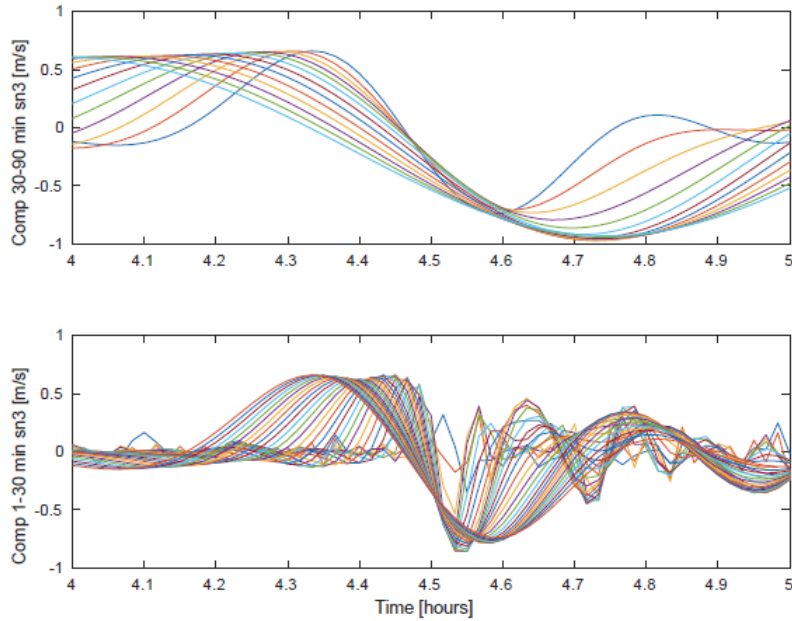


Fig. 5.26: Time evolution of CWT coefficients in time interval 4-5 UTC: period range  $[30 \div 90]$  min in the upper panel, period range  $[1 \div 30]$  min in the lower panel.

Fig. 5.26, which shows the time evolution of all scale CWT coefficients, highlights the contributions at different scales. The wavelets with longer period, between 30 and 90 minutes (top plot in Fig. 5.26), have minimum values between 4:35 and 4:45 and characterize particularly the evolution of the long transient after the collision. The plot reported in the bottom of Fig. 5.26, instead, shows the contributions of the scales between 1 and 30 minutes. All of these CWT coefficient have maximum values between 4:20 and 4:30 followed by a minimum between 4:30 and 4:35. The sum of these contributions, along with the contributions of longer wavelets, reconstruct accurately the collision between the two air fronts.

The values of the CWT coefficients after the collision highlight the contributions of different phenomena and their time scales. The plot at the top of Fig. 5.26 shows that, after had reached the minimum values, the CWT coefficients grew with a constant rate. This contribution with a long time scale is the physical mechanism driving the katabatic flow that slowly returns to the stable regimes (see  $u$  profile in Fig. 5.25 from 4:30 to 5:30). Thus, collision was not powerful enough to definitively modify the flow. In this plot it is also interesting to note that the CWT coefficient for the wavelet having a 30 minutes period (blue line) had a maximum at 4:50 and quickly decayed. This represents the time scale of one of the internal waves of the post-collision regime. These oscillations are also represented in the bottom plot of Fig. 5.26 by the CWT coefficients of the wavelet with period 20-30 minutes. In this plot, and also in the contour plot of Fig. 5.25, can be also noted a group of wavelet having period about 15 minutes and amplitudes around 0.3 m/s which decayed with a lower rate and are visible until 6:00. These dampened oscillations are an effect of the collision front that is dissipating its energy. Wavelets with even shorter period (5-10 minutes) also had higher amplitudes after the collision than they had before

it. This is an effect of the turbulence generated by the mixing of the fronts and slowly decayed.

## 5.4 30 September

An in-depth analysis was carried out also for Day 274 (September 30). Results indicate that Day 274 exhibits many of the flow patterns and characteristics observed also for Day 272, as summarized in the following.

Fig. 5.27 the wind direction registered by sonic anemometers installed at 10 m in each tower.

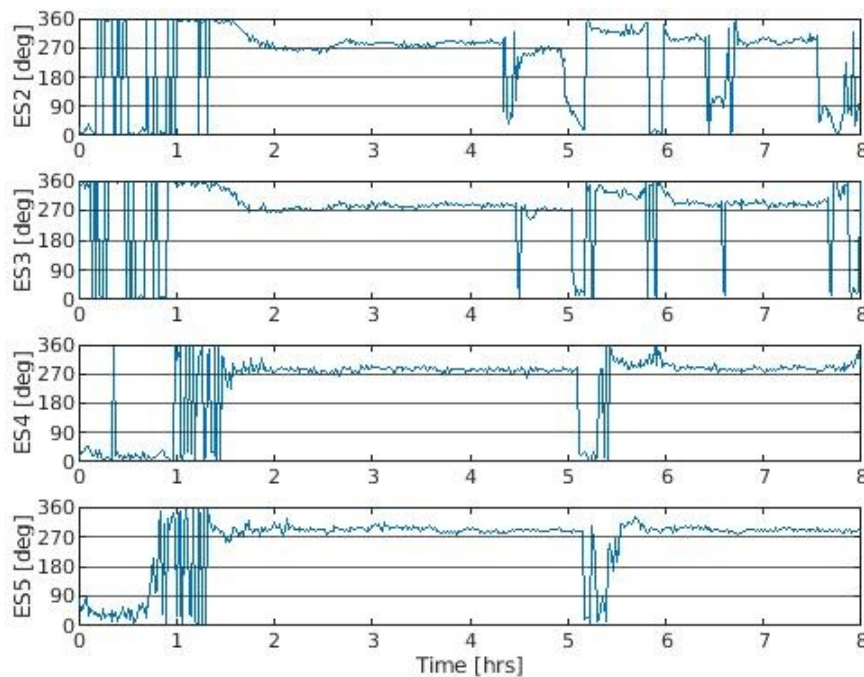


Fig. 5.27: Wind direction for day 274 for towers ES2-ES5.

Comparing Fig. 5.7 and 5.27, it is easy to notice the similarities between the wind direction behavior on day 272 and 274. Also in this case the three different flow regimes are distinguishable, in particular *evening transition* regime before the "pure" *downslope flow* onset at 2 UTC, which lasts until a powerful perturbation occurs thus demarcating the beginning of *collision region*. At tower ES2, the collision occurs approximately at the same time as for day 272 (4:30 UTC). However, in this case the time delay between the occurrence at ES2 and the other three towers is larger and equal to almost a hour between ES5 and ES2. This suggested a slower velocity propagation of the valley front along the slope.

Also for day 274 values of oscillation period deriving from relation  $p = N \sin \alpha$  were calculated, discriminating the two atmospheric layers characterized by different stability (as before, lower layer is indicated with 1-3 and upper layer with 3-5). The

temporal evolution of the two series of computed  $N^2$  and corresponding periods at tower ES5 are represented in Fig. 5.28.

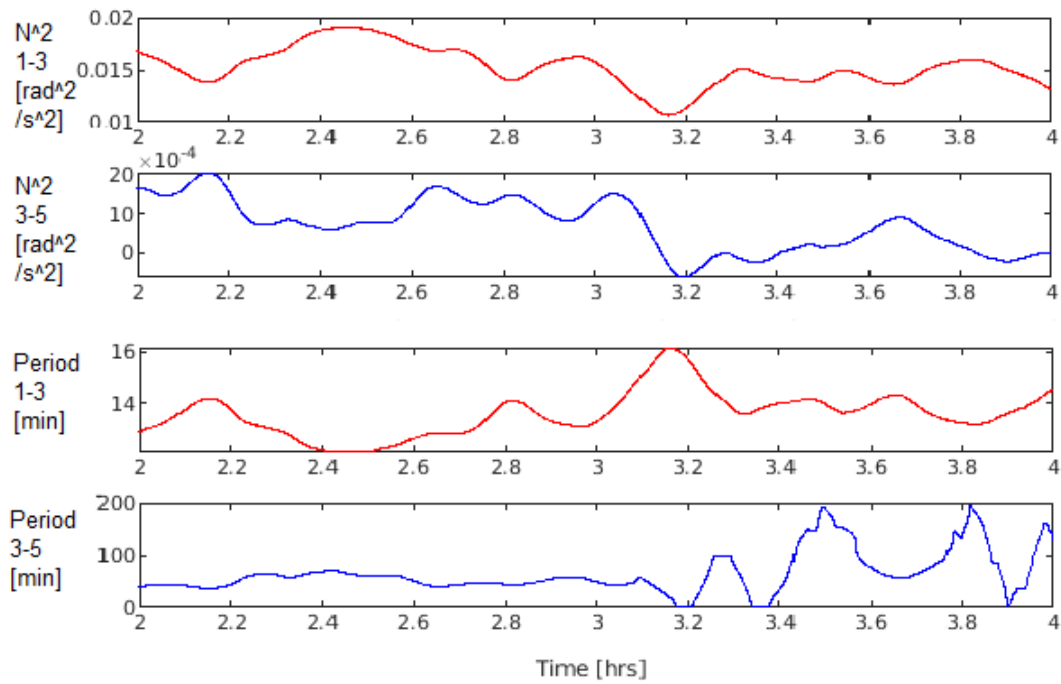


Fig. 5.28:  $N^2$  and corresponding periods during interval 2-4 UTC at tower ES5.  $N^2$  1-3 refers to the low layer, while  $N^2$  3-5 to the higher one. The same holds for periods.

Values obtained for periods are almost identical to those retrieved for 272, with  $p$  varying between 12 and 16 minutes for the lower layer. For the upper layer,  $p$  is near to 60 minutes for the initial part of the time interval, and larger after 3 UTC.

In the interval 2-4 UTC,  $u$  component oscillations with period near to 25 minutes were detected at 10 m (sonic 4) at tower ES5 by wavelet method, as shown in Fig. 5.29.

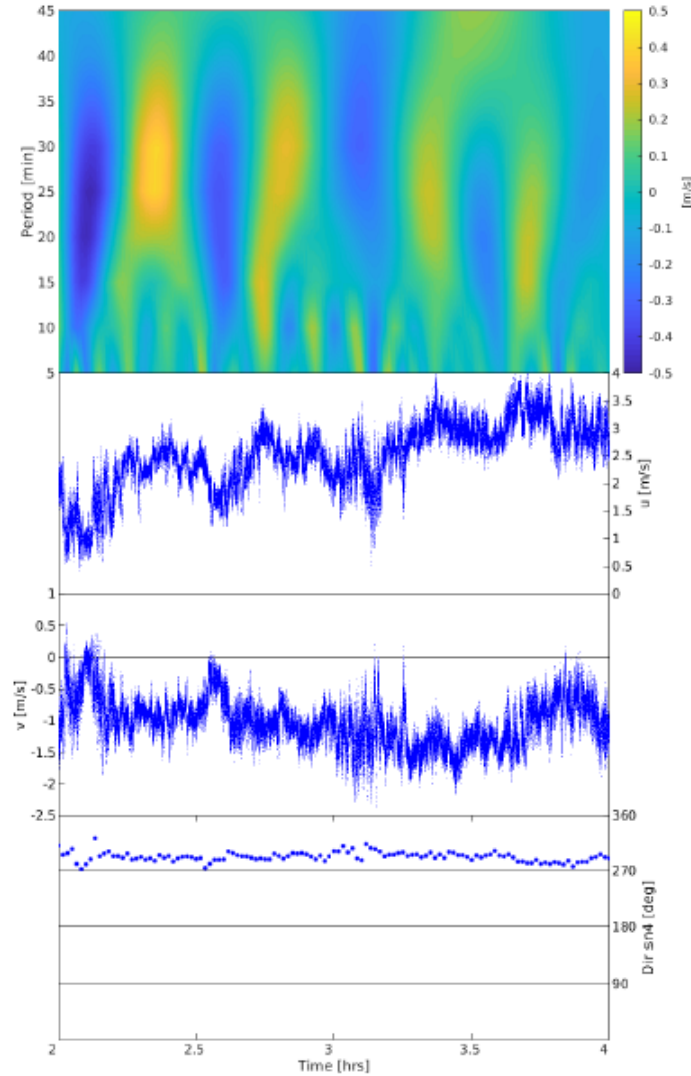


Fig. 5.29: CWT contour plot for  $u$  component with period ranging from 5 to 45 minutes,  $u$  component time-series,  $v$  component time-series and wind direction. Plot refers to sonic 4 (at 10 m) of ES5.

Wavelet coefficients reached maximum values of 0.4 m/s in correspondence of  $p = 25$  minutes. For tower ES5 this behavior was detected also at 20 m, while it was not visible at lower levels. As for day 272, discrepancy was found with  $N$ -related periodic oscillation, suggesting that also in this occasion the phenomenon cannot be ascribed to the theory of downslope flow internal oscillations discussed in Chapter 2.

One example regarding wavelet analysis application to collision event has been reported. As for day 272, wavelet transform coefficient plot for sonic 3 (5 m) of tower ES5 is presented (Fig. 5.30).

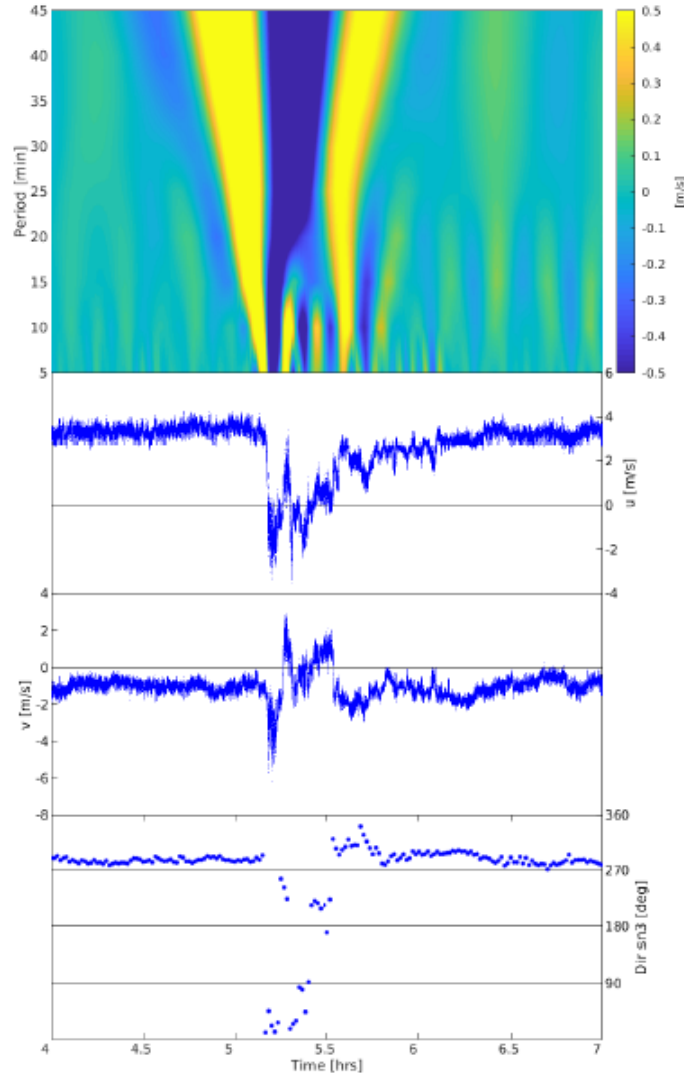


Fig. 5.30: CWT contour plot for  $u$  component with period ranging from 5 to 45 minutes,  $u$  component time-series,  $v$  component time-series and wind direction. Plot refers to sonic 3 (at 5 m) of ES5.

Also in this case collision was detected through wavelet methods observing a time-localized band of high intensity transform coefficients for all frequencies. Velocity  $u$  component abruptly varied from 4 to -2 m/s at 5:10 UTC, with subsequent perturbations in the flow which lasted until 6:00 UTC, when katabatic flow regime was restored. Particularly high coefficients values were achieved by the high frequency (period smaller than 10 minutes) oscillations originated immediately after the collision, when the mixing among the two flows occurred. The period between the collision and the restoring of the downslope flow was shorter in 274 than in 272; in its final part there was a relevant variation of velocity field (which is easy to note in the time series for the  $v$  component) highlighted by a high value of CWT coefficient at all frequencies.

# Chapter 6

## Conclusion

Downslope flows over irregular topography have been an intensively studied research object during the last two decades. Interest in achieving a complete understanding about these phenomena has expanded particularly over the last years, due to the increasing demand of reliable numerical weather prediction models related to complex terrain configurations.

Following some recent works related to this topic, in this thesis project downslope flows have been investigated by using an advanced analysis method, the wavelet transform. This mathematical tool has found several applications in various research fields due to its remarkable capacity to examine signals in time/space and frequency domain simultaneously.

Through the wavelet transform method a specific dataset has been studied, consisting of a subset of MATERHORN 2012 experimental campaign, which has been chosen for the highly detailed measurement networks it was composed of. In particular, 8 hours interval during nighttime of days 28 and 30 September 2012 has been selected as object of the analysis following the observations of [24], with the purpose of estimating the ability of the aforementioned method in detecting downslope flows characteristics and time evolution.

Relevant results were obtained from the study, in particular for day 28 September. Three different flow regimes were identified and analyzed in detail: evening transition, "pure" downslope regime and collision region. The first one was related to the passage from the daytime wind circulation to a downslope nocturnal flow, with alignment of wind directions along downslope. Change in direction occurred following the descent of the slope, according to the hypothesis of "stagnation front" cited in [17]. Identification of this transient region was described by low frequency features in wavelet transform plots, which are mathematical abstraction resulting by the procedure followed by wavelets to reconstruct signals. "Pure" downslope regime was characterized by typical "nose" shapes in wind velocity profiles, with peaks registered at 2-5 m above the ground. Oscillations with period of 8 minutes were detected through the wavelet method during this temporal range at the observation site located at the top of the slope. This value was found in disagreement with the one of type  $p = N \sin \alpha$  predicted by [42]. Oscillations with period equal to 20 minutes were detected at towers located at lower segments of the slope, and they were attributed to the interaction between downslope flow and valley wind circulation,

in agreement with the observation of [41]. Collision region represented the collision between downslope flow and a front coming from the surrounding valley. Wavelet transform was able to reveal it through a time-localized band of high intensity transform coefficients at all frequencies. Wavelet method also identified the presence of inner oscillations during the perturbed flow generated after the collision, divided in high frequency fluctuations related to turbulent mixing, dampened oscillations deriving from the dissipation of collision front energy and a contribution of lower frequencies internal waves due to the restoring of the downslope regime. It was also observed that the collision was not powerful enough to irreversibly modify the flow, because the downslope regime established again after one hour.

Similarities were noticed for day 30 September, which was separable into the same three regions. Oscillations with period equal to 25 minutes were recognized during the "pure" downslope regime, and also in this case discrepancy with  $N$ -dependent theoretical period was found. Wavelet analysis allowed to determine the existence of the collision through a narrow band with considerably high coefficient values.

Ability of wavelet transform tool in capturing the features of downslope flows has been tested, providing remarkable results. However, the complex nature of downslope flows implies that further studies will be essential to provide a more and more accurate description of these phenomena. The extension to this analysis to a larger databases, including both other physical variables and measurement sites, would allow a deeper characterization of the events and the link to physical phenomena. In agreement with the procedure of [12], wavelet transform coefficient of cross-correlation of velocity components and temperature could be computed in order to evaluate the ability of this method to characterize, for example, heat fluxes in the proximity of the collision event. It would also be interesting to investigate more in detail the collision event, trying to describe its features, like the penetration depth of the incoming valley front, and potential spikes in turbulent kinetic energy which could be linked to the interaction between the downslope and the valley flow. Moreover, high frequency studies could be performed by using wavelets as high-pass filters, in order to explore in-depth turbulent related aspects of the downslope flows.

# Bibliography

- [1] Materhorn-X final data archive. <https://data.eol.ucar.edu/project/MATERHORN-X>.
- [2] O. Acevedo, G. A Degrazia, F. Puhales, L. Martins, P. Oliveira, C. Teichrieb, S. Silva, R. Maroneze, B. Bodmann, L. Mortarini, et al. Monitoring the micro-meteorology of a coastal site next to a thermal power plant from the surface to 140 m. *Bulletin of the American Meteorological Society*, 99(4):725–738, 2018.
- [3] P. Addison. *The illustrated wavelet transform handbook: introductory theory and applications in science, engineering, medicine and finance*. CRC press, 2017.
- [4] S. Al-Yahyai, Y. Charabi, and A. Gastli. Review of the use of numerical weather prediction (nwp) models for wind energy assessment. *Renewable and Sustainable Energy Reviews*, 14(9):3192–3198, 2010.
- [5] G. Amanatidis, K. Papadopoulos, J. Bartzis, and C. Helmis. Evidence of katabatic flows deduced from a 84 m meteorological tower in athens, greece. *Boundary-Layer Meteorology*, 58(1-2):117–132, 1992.
- [6] S. Axelsen and H. van Dop. Large-eddy simulation of katabatic winds. part 1: Comparison with observations. *Acta Geophysica*, 57(4):803–836, 2009.
- [7] W. Blumen. *Atmospheric processes over complex terrain*, volume 23. Springer, 2016.
- [8] S. Bozhokin, I. Suslova, and D. Tarakanov. Elimination of boundary effects at the numerical implementation of continuous wavelet transform to nonstationary biomedical signals. 2019.
- [9] P. Burman, T. Prabha, R. Morrison, and A. Karipot. A case study of turbulence in the nocturnal boundary layer during the indian summer monsoon. *Boundary-layer meteorology*, 169(1):115–138, 2018.
- [10] J. Businger and K. Rao. The formation of drainage wind on a snow-dome. *Journal of Glaciology*, 5(42):833–841, 1965.
- [11] M. Buzzi. *Challenges in operational numerical weather prediction at high resolution in complex terrain*. PhD thesis, ETH Zurich, 2008.

- [12] D. Cava, L. Mortarini, U. Giostra, R. Richiardone, and D. Anfossi. A wavelet analysis of low-wind-speed submeso motions in a nocturnal boundary layer. *Quarterly Journal of the Royal Meteorological Society*, 143(703):661–669, 2017.
- [13] J. Cuxart, C. Yagüe, G. Morales, E. Terradellas, J. Orbe, J. Calvo, A. Fernández, M. Soler, C. Infante, P. Buenestado, et al. Stable atmospheric boundary-layer experiment in spain (sables 98): a report. *Boundary-layer meteorology*, 96(3):337–370, 2000.
- [14] I. Daubechies. *Ten lectures on wavelets*, volume 61. Siam, 1992.
- [15] M. Farge. Wavelet transforms and their applications to turbulence. *Annual review of fluid mechanics*, 24(1):395–458, 1992.
- [16] H. Fernando, E. Pardyjak, S. Di Sabatino, F. Chow, S. De Wekker, S. Hoch, J. Hacker, J. Pace, T. Pratt, Z. Pu, et al. The materhorn: Unraveling the intricacies of mountain weather. *Bulletin of the American Meteorological Society*, 96(11):1945–1967, 2015.
- [17] H. Fernando, B. Verhoef, S. Di Sabatino, L. Leo, and S. Park. The phoenix evening transition flow experiment (transflex). *Boundary-layer meteorology*, 147(3):443–468, 2013.
- [18] R. Fleagle. A theory of air drainage. *Journal of Meteorology*, 7(3):227–232, 1950.
- [19] D. Gabor. Theory of communication. part 1: The analysis of information. *Journal of the Institution of Electrical Engineers-Part III: Radio and Communication Engineering*, 93(26):429–441, 1946.
- [20] M. Gallegati. A wavelet-based approach to test for financial market contagion. *Computational Statistics & Data Analysis*, 56(11):3491–3497, 2012.
- [21] N. Gamage and W. Blumen. Comparative analysis of low-level cold fronts: Wavelet, fourier, and empirical orthogonal function decompositions. *Monthly weather review*, 121(10):2867–2878, 1993.
- [22] R. Ganesan, T. Das, and V. Venkataraman. Wavelet-based multiscale statistical process monitoring: A literature review. *IIE transactions*, 36(9):787–806, 2004.
- [23] J. Garratt. The atmospheric boundary layer. *Earth-Science Reviews*, 37(1-2):89–134, 1994.
- [24] A. Grachev, L. Leo, S. Di Sabatino, H. Fernando, E. Pardyjak, and C. Fairall. Structure of turbulence in katabatic flows below and above the wind-speed maximum. *Boundary-layer meteorology*, 159(3):469–494, 2016.
- [25] A. Grossmann, R. Kronland-Martinet, and J. Morlet. Reading and understanding continuous wavelet transforms. In *Wavelets*, pages 2–20. Springer, 1990.

- [26] A. Grossmann and J. Morlet. Decomposition of hardy functions into square integrable wavelets of constant shape. *SIAM journal on mathematical analysis*, 15(4):723–736, 1984.
- [27] C. Hocut. *Multi-scale flow and turbulence in complex terrain under weak synoptic conditions*. University of Notre Dame, 2013.
- [28] T. Horst and J. Doran. Nocturnal drainage flow on simple slopes. *Boundary-Layer Meteorology*, 34(3):263–286, 1986.
- [29] J. Howell and L. Mahrt. Multiresolution flux decomposition. *Boundary-Layer Meteorology*, 83(1):117–137, 1997.
- [30] J. Kaimal and J. Finnigan. *Atmospheric boundary layer flows: their structure and measurement*. Oxford university press, 1994.
- [31] M. Lehner, C. Whiteman, S. Hoch, D. Jensen, E. Pardyjak, L. Leo, S. Di Sabatino, and H. Fernando. A case study of the nocturnal boundary layer evolution on a slope at the foot of a desert mountain. *Journal of Applied Meteorology and Climatology*, 54(4):732–751, 2015.
- [32] A. Lewis and G. Knowles. Image compression using the 2-d wavelet transform. *IEEE Transactions on image Processing*, 1(2):244–250, 1992.
- [33] P. Liu. Wavelet spectrum analysis and ocean wind waves. In *Wavelet Analysis and Its Applications*, volume 4, pages 151–166. Elsevier, 1994.
- [34] P. Manins and B. Sawford. A model of katabatic winds. *Journal of the Atmospheric Sciences*, 36(4):619–630, 1979.
- [35] S. Meyers, B. Kelly, and J. O’Brien. An introduction to wavelet analysis in oceanography and meteorology: With application to the dispersion of yanai waves. *Monthly weather review*, 121(10):2858–2866, 1993.
- [36] J. Morlet. Sampling theory and wave propagation. In *Issues in acoustic Signal—image processing and recognition*, pages 233–261. Springer, 1983.
- [37] L. Mortarini, D. Cava, U. Giostra, O. Acevedo, L. Nogueira Martins, P. Soares de Oliveira, and D. Anfossi. Observations of submeso motions and intermittent turbulent mixing across a low level jet with a 132-m tower. *Quarterly Journal of the Royal Meteorological Society*, 144(710):172–183, 2018.
- [38] L. Mortarini, E. Ferrero, S. Falabino, S. Castelli, R. Richiardone, and D. Anfossi. Low-frequency processes and turbulence structure in a perturbed boundary layer. *Quarterly Journal of the Royal Meteorological Society*, 139(673):1059–1072, 2013.
- [39] S. Mousavi and C. Langston. Hybrid seismic denoising using higher-order statistics and improved wavelet block thresholding. *Bulletin of the Seismological Society of America*, 106(4):1380–1393, 2016.

- [40] V. Pichot, J. Gaspoz, S. Molliex, A. Antoniadis, T. Busso, F. Roche, F. Costes, L. Quintin, J. Lacour, and J. Barthélémy. Wavelet transform to quantify heart rate variability and to assess its instantaneous changes. *Journal of Applied Physiology*, 86(3):1081–1091, 1999.
- [41] W. Porch, W. Clements, and R. Coulter. Nighttime valley waves. *Journal of Applied Meteorology*, 30(2):145–156, 1991.
- [42] M. Princevac, J. Hunt, and H. Fernando. Quasi-steady katabatic winds on slopes in wide valleys: Hydraulic theory and observations. *Journal of the Atmospheric Sciences*, 65(2):627–643, 2008.
- [43] J. Rees, W. Staszewski, and J. Winkler. Case study of a wave event in the stable atmospheric boundary layer overlying an antarctic ice shelf using the orthogonal wavelet transform. *Dynamics of atmospheres and oceans*, 34(2-4):245–261, 2001.
- [44] C. Román-Cascón, C. Yagüe, L. Mahrt, M. Sastre, G. Steeneveld, E. Pardyjak, A. Boer, and O. Hartogensis. Interactions among drainage flows, gravity waves and turbulence: a blast case study. *Atmospheric Chemistry and Physics*, 15(15):9031–9047, 2015.
- [45] J. Rottman and R. Smith. A laboratory model of severe downslope winds. *Tellus A*, 41(5):401–415, 1989.
- [46] U. Schumann. Large-eddy simulation of the up-slope boundary layer. *Quarterly Journal of the Royal Meteorological Society*, 116(493):637–670, 1990.
- [47] E. Skillingstad. Large-eddy simulation of katabatic flows. *Boundary-layer meteorology*, 106(2):217–243, 2003.
- [48] E. Strang and H. Fernando. Entrainment and mixing in stratified shear flows. *Journal of Fluid Mechanics*, 428:349–386, 2001.
- [49] K. Strobach. Unser planet erde. 1991.
- [50] J. Sun. Tilt corrections over complex terrain and their implication for co<sub>2</sub> transport. *Boundary-layer meteorology*, 124(2):143–159, 2007.
- [51] H. Suzuki, T. Kinjo, Y. Hayashi, M. Takemoto, K. Ono, and Y. Hayashi. Wavelet transform of acoustic emission signals. *Journal of acoustic emission*, 14:69–84, 1996.
- [52] F. Tampieri. *Turbulence and dispersion in the planetary boundary layer*. Springer, 2017.
- [53] E. Terradellas, G. Morales, J. Cuxart, and C. Yagüe. Wavelet methods: application to the study of the stable atmospheric boundary layer under non-stationary conditions. *Dynamics of Atmospheres and Oceans*, 34(2-4):225–244, 2001.
- [54] E. Terradellas, M. Soler, E. Ferreres, and M. Bravo. Analysis of oscillations in the stable atmospheric boundary layer using wavelet methods. *Boundary-layer meteorology*, 114(3):489–518, 2005.

- [55] C. Torrence and G. Compo. A practical guide to wavelet analysis. *Bulletin of the American Meteorological society*, 79(1):61–78, 1998.
- [56] S. Viana, E. Terradellas, and C. Yagüe. Analysis of gravity waves generated at the top of a drainage flow. *Journal of the Atmospheric Sciences*, 67(12):3949–3966, 2010.
- [57] D. Vickers and L. Mahrt. Quality control and flux sampling problems for tower and aircraft data. *Journal of atmospheric and oceanic technology*, 14(3):512–526, 1997.
- [58] H. Weng and W. Lau. Wavelets, period doubling, and time–frequency localization with application to organization of convection over the tropical western pacific. *Journal of the atmospheric sciences*, 51(17):2523–2541, 1994.
- [59] C. Whiteman. *Mountain meteorology: fundamentals and applications*. Oxford University Press, 2000.
- [60] C. Whiteman and S. Zhong. Downslope flows on a low-angle slope and their interactions with valley inversions. part i: Observations. *Journal of Applied Meteorology and Climatology*, 47(7):2023–2038, 2008.
- [61] N. Wood. Wind flow over complex terrain: a historical perspective and the prospect for large-eddy modelling. *Boundary-Layer Meteorology*, 96(1-2):11–32, 2000.
- [62] D. Zardi and C. Whiteman. Diurnal mountain wind systems. In *Mountain Weather Research and Forecasting*, pages 35–119. Springer, 2013.

# Ringraziamenti

Innanzitutto desidero ringraziare la Prof.ssa Silvana Di Sabatino per aver accettato di farmi da relatore ed per aver supervisionato il mio lavoro.

Ringrazio enormemente la Dott.ssa Laura S. Leo e il Dott. Temistocle Grenga per avermi supportato e sopportato durante questi mesi, dimostrando infinita professionalità e disponibilità nel guidarmi attraverso la realizzazione di questo progetto.

Ringrazio il Dipartimento di Fisica e Astronomia dell'Università di Bologna e l'Università Tecnica di Aquisgrana (RWTH), in particolare nella persona del Prof. Dr.-Ing. Heinz Pitsch, per avermi dato l'opportunità di lavorare in un istituto di ricerca tra i più rinomati a livello mondiale, contribuendo in modo notevole all'arricchimento della mia formazione.

Ringrazio il Dott. Antonio Attili per i preziosi consigli e per l'interesse manifestato nei confronti di questo lavoro.

Infine, l'ultimo e più importante ringraziamento va ai miei genitori, che mi hanno sostenuto in ogni modo, e a tutte le persone che mi sono state vicino durante questo lungo percorso, senza le quali nulla sarebbe stato possibile.